PSFC/RR-99-11 DOE/ET-54512-333

H-α/D-α Spectroscopy on Alcator C-Mod

T.E. Tutt

Plasma Science and Fusion Center
Massachusetts Institute of Technology
Cambridge, MA 02139

September 1999

This work was supported by the U. S. Department of Energy Contract No. DE-FC002-99ER54512. Reproduction, translation, publication, use and disposal, in whole or in part by or for the United States government is permitted.

H-α/D-α Spectroscopy on Alcator C-Mod

by

Teresa Elizabeth Tutt

B.S., Engineering Physics (1997)
Rensselaer Polytechnic Institute

Submitted to the Department of Nuclear Engineering
in partial fulfillment of the requirements for the degree of

Master of Science

at the

MASSACHUSETTS INSTITUTE OF TECHNOLOGY

September 1999

Author ..... Teresa E. Tutt
Department of Nuclear Engineering
September 10, 1999

Certified by 9/30/99
Earl S. Marmar
Research Scientist
Thesis Supervisor

Certified by ..... I. H. Hutchinson
Ian H. Hutchinson
Professor of Nuclear Engineering, Head of Alcator Project
Thesis Reader

Accepted by .....
Prof. Jeffrey Freidberg
Chairman, Departmental of Nuclear Engineering

H-α/D-α Spectroscopy on Alcator C-Mod

by

Teresa Elizabeth Tutt

Submitted to the Department of Nuclear Engineering
on September 10, 1999, in partial fulfillment of the
requirements for the degree of
Master of Science

Abstract

A high-resolution optical spectrometer has been recently implemented on the Alcator C-Mod tokamak to measure the neutral hydrogen/deuterium (H/D) ratio at the plasma edge. The spectrometer determines the ratio by observing Balmer-α transitions of each species. Auxiliary heating of plasma in the Alcator C-Mod tokamak is accomplished by means of D(H) minority ICRF. Wave absorption is a sensitive function of the minority concentration, and kinetic theory predicts a critical value for which the single-pass RF absorption is maximum. All shots up to the present have employed passive control of the H/D ratio by means of baking, electron cyclotron discharge cleaning (ECDC), and boronization of the vacuum vessel prior to a run. Minority (hydrogen) concentrations have been measured as low as 2%. Since kinetic theory predicts a critical value of $\sim$ 5% for these shots, this presents an opportunity to compare theory with experiment. Recent measurements have been made of plasma stored energy vs. minority concentration. For a given RF power input and constant plasma current, experiment agrees fairly well with theory.

Thesis Supervisor: Earl S. Marmar
Title: Research Scientist

Acknowledgments

Faculty: Prof. Earl Marmar, Prof. Jeff Freidberg, Prof. Ambrogio Fasoli, Prof. Ricardo Betti, Prof Ian Hutchinson

Staff: Dr. John Rice, Dr. Jim Terry, Ms. Clare Egan, Ms. Marsha Levine, Ms. Mary McPeak. Mr. Frank Silva, Ms. Valerie Censabella

Students: Jim Reardon, Maxim Umansky, Rob Nachtrieb, Cindy Christensen, Shan-Yuan Ho

For Ruup

Contents

List of Figures

Chapter 1

Purpose

We have implemented an optical spectrometer on Alcator C-Mod for the purpose of measuring the ratio between the two naturally occuring isotopes of hydrogen: ordinary, or "light" hydrogen (^{1}H); and "heavy" hydrogen, or deuterium (^{2}H or simply D). The hydrogen/deuterium ratio is important, particularly as it relates to auxiliary plasma heating.

Supplementary heating of plasma is accomplished by means of Radio Frequency (RF) heating in the Ion Cyclotron Range of Frequencies (ICRF). The resonant cyclotron frequency is given by:

$$\omega_{c_i} = \frac{|q|B}{m_i} \tag{1.1}$$

where $|q|$ is the charge in coulombs (C), B is tne magnetic field in Teslas (T), and m_i is the mass of the ion in kg. In a magnetic field of 5.4 T the resonant frequencies are 80 MHz and 40 MHz for protons (H^+) and deuterons (D^+), respectively.

Standard shots use a deuterium plasma with hydrogen as the minority ion species. High field shots ($\sim$ 8 T on axis), use ^{3}He ions as a minority ion species, as they are also resonant at 80 MHz in the 8 T field. All other parameters being equal, the single-pass RF wave absorption and sububsequent stored energy increase of the plasma is highly dependent on the concentration of the minority ion species.

This thesis discusses measurement of the hydrogen/deuterium ratio by means of

optical spectroscopy. A brief background on minority RF heating is presented, followed by detailed descrition of the spectrometer setup, alignment and calibration. Interpretation and applications of the spectrometer data are discussed in this section as well. Section four discusses actual experimental data and effects of machine conditions on the H/D ratio. Finally, the effects of the ratio on RF absorption are explored.

Chapter 2

Background: Minority ICRF Heating

Alcator C-Mod employs a "fast" magnetosonic (compressional Alfvén) wave launched into the plasma via antennas mounted on the outboard (low field) side of the plasma. Since the toroidal field ($\mathbf{B}_\phi$) varies as 1/R, then $\omega_c = \omega_c(R)$ and the resonant region is localized where $\omega_{RF} = \omega_c(R)$.

Compressional Alfvén waves are used as they can propagate across the toroidal magnetic field lines. Shear Alfvén waves are not suitable as they will not propagate above the ion cyclotron frequency and therefore must be launched from the high field (inboard) side of the plasma. Further, such waves undergo mode conversion to electrostatic waves at the plasma edge, preventing further propagation in the plasma.

Propagation of fast magnetosonic waves in the plasma is determined by the dispersion relation:

$$\begin{bmatrix} D_{xx} & D_{xy} & D_{xz} \\ D_{yx} & D_{yy} & D_{yz} \\ D_{zx} & D_{zy} & D_{zz} \end{bmatrix} \cdot \begin{bmatrix} E_x \\ E_y \\ E_z \end{bmatrix} = 0 \tag{2.1}$$

which is is a function of the refractive index (N) in the parallel ($||$), and perpendicular

($\perp$) directions. The dispersion matrix, $\overline{\overline{\mathbf{D}}}$, is given by:

$$\overline{\overline{\mathbf{D}}} = \begin{vmatrix} -N_{||}^2 + S & -iD & N_{||}N_{\perp} \\ iD & -N_{||}^2 + N_{\perp}^2 + S & 0 \\ N_{||}N_{\perp} & 0 & N_{\perp}^2 + p \end{vmatrix} \tag{2.2}$$

with:

$$S = 1 - \sum_{\alpha} \frac{\omega_{p_\alpha}^2}{\omega^2 - \omega_{c_\alpha}^2}$$

$$D = \sum_{\alpha} \frac{\omega_{c_\alpha}}{\omega} \frac{\omega_{p_\alpha}^2}{\omega^2 - \omega_{c_\alpha}^2}$$

$$p = 1 - \sum_{\alpha} \frac{\omega_{p_\alpha}^2}{\omega^2}$$

where the summation is over the electrons and ion species of the plasma. (The sign of the charge is included in the cyclotron frequencies, ω_c for the "D" term).

Non-trivial solutions for equation 2.1 exist when $\left|\overline{\overline{\mathbf{D}}}\right| = 0$. Since $N_{||}$ is known, then:

$$\left|\overline{\overline{\mathbf{D}}}\right| = aN_{\perp}^4 - bN_{\perp}^2 + c = 0 \tag{2.3}$$

where:

$$a = S, \;\; b = (p - N_{||}^2)(S + p) - D^2, \;\; c = p[(p - N_{||}^2)^2 - D^2]$$

It follows that:

$$N_{\perp}^2 = \frac{b \pm \sqrt{b^2 - 4ac}}{2a} \tag{2.4}$$

by the quadratic formula. The positive quadratic solution to eq 2.4 is associated with the lower hybrid, or "slow" wave regime, while the negative quadratic solution represents the magnetosonic, or "fast" wave regime.[1]

2.1 Ion Cyclotron Resonance Heating of Minority Species in a Two-Ion Plasma

Typically, Alcator has utilized the fast wave (FW) regime for IDCRF heating. LHW's are typically used for other applications, such as the equilibrium current drive.

The refractive index perpendicular to the magnetic field is therefore represented by:

$$N_\perp^2 = \frac{(S - N_{||}^2)^2 - D^2}{S - N_{||}^2} = \frac{(R - N_{||}^2)(L - N_{||}^2)}{S - N_{||}^2} \tag{2.5}$$

Where:

$$R = S + D \quad (\text{right} - \text{hand polarization}) \tag{2.6}$$

$$L = S - D \quad (\text{left} - \text{hand polarization}) \tag{2.7}$$

Since ion frequencies dominate the dispersion relation, then the resonances where:

$$S \to \left| \frac{\omega_{p_i}^2}{\omega^2 - \omega_{c_i}^2} \right| \to \infty \tag{2.8}$$

$$D \to \left| \frac{\omega_{c_i}}{\omega} \frac{\omega_{p_i}^2}{\omega^2 - \omega_{c_i}^2} \right| \to \infty \tag{2.9}$$

occur when the RF frequency approaches the ion cyclotron resonance frequency $\omega \to \omega_{c_i}$. From eq. 2.4 one finds:

$$\frac{E_x}{E_y} = \frac{iD}{S - N_{||}^2} \to \frac{iD}{S} \sim \frac{i\omega_{c_i}}{\omega} \sim +i \tag{2.10}$$

This means the wave is right hand circularly polarized (RHCP) which is in the same direction as *electron* rotation. This is undesirable, as effective ion cylotron damping of the wave (and resultant heating) requires left hand circular polarization (LHCP), which is in the direction of *ion* rotation.

One possible solution is to use a harmonic of this frequency. Damping is proportional to $(k_\perp \rho_{L_i})^{n-1}$, where n is the frequency harmonic. The difficulty with this

approach is that since damping is proportional to the Larmor radius, ρ_{L_i} (which is in turn proportional to the ion energy), typically only ions in the tail of the distribution function are heated in this scheme.

A more practical approach, however, is to add a small amount of a different ion species. Polarization direction is still dominated by the majority ion frequency, but there is a component of polarization rotating with the minority ions, to provide heating.[2]

RF absorption by the minority ions is then determined by the fraction of left hand polarization[3]:

$$\frac{|E_L|^2}{|E_Y|^2} = \frac{(\frac{\omega}{\omega_i} - 1)^2(\frac{\omega}{\omega_i} - \frac{N_{||}^2}{N^2})^2}{(\frac{\omega}{\omega_i})^2(1 + \frac{N_{||}^2}{N^2})^2} \tag{2.11}$$

and the amount of RF damping is then:

$$\text{RF Absorption} = 1 - e^{2\epsilon} \tag{2.12}$$

where:

$$2\epsilon = \frac{|E_L|^2}{|E_Y|^2} \frac{\omega_{p_i}}{c} \frac{n_{min}}{n_{Maj}} \frac{Z_{min} m_{Maj}}{Z_{Maj} m_{min}} R_o \tag{2.13}$$

2.2 Kinetic Theory Prediction of Critical Minority Ion Concentration

It is desirable to maximize RF heating by determining an optimum minority/majority ion concentration. First we consider the resonance condition according to Fluid Theory. From eq. 2.4, we obtain the fast wave dispersion relation:

$$N_\perp^2 = \frac{\left[\sum_j \frac{\omega_{p_j}^2}{\omega_{c_j}(\omega+\omega_{c_j})} - N_{||}^2\right]\left[\sum_j \frac{\omega_{p_j}^2}{\omega_{c_j}(\omega-\omega_{c_j})} + N_{||}^2\right]}{\left[\sum_j \frac{\omega_{p_j}^2}{\omega^2-\omega_{c_j}^2} + N_{||}^2\right]} \tag{2.14}$$

From the denominator, one finds the resonance condition:

$$-\frac{\omega_{p_e}^2}{\omega_{c_e}^2} + \frac{\omega_{p_{Maj}}^2}{\omega^2 - \omega_{c_{Maj}}^2} + \frac{\omega_{p_{min}}^2}{\omega^2 - \omega_{c_{min}}^2} + N_{||}^2 = 0 \tag{2.15}$$

where subscripts Maj and min represent the majority and minority ions, respectively. Corresponding cutoffs occur where the left and right bracket expressions of the numerator go to zero. As before, the electron frequency can be neglected. The resonance condition then reduces to:

$$\frac{\omega_{p_{Maj}}^2}{\omega^2 - \omega_{c_{Maj}}^2} + \frac{\omega_{p_{min}}^2}{\omega^2 - \omega_{c_{min}}^2} - N_{||}^2 = 0 \tag{2.16}$$

To determine whether Fluid Theory is sufficient to describe the heated plasma in this case, we apply the kinetic theory equation[4]:

$$\frac{\omega_{p_{Maj}}^2}{\omega^2 - \omega_{c_{Maj}}^2} + \frac{\omega_{p_{min}}^2}{2\sqrt{2}k_{||}v_{th}\omega}\left[Z(\zeta_{min}^-) + Z(\zeta_{min}^+)\right] - N_{||}^2 = 0 \tag{2.17}$$

where $Z(\zeta)$ is the plasma dispersion function, defined as:

$$Z(\zeta) = \frac{1}{\sqrt{\pi}}\int_C \frac{e^{-t^2}}{t-\zeta}dt \tag{2.18}$$

or:

$$Z(\zeta) = -2e\int_0^z e^{t^2}dt + i\sqrt{\pi}e^{-z^2} \tag{2.19}$$

with:

$$\zeta_m^{\pm} = \frac{\omega \pm \omega_{c_{min}}}{\sqrt{2}k_{||}v_{th_{min}}}$$

Integration is carried out over the Landau contour. For a cold plasma, $|\zeta| >> 1$, the complex component may be neglected and $Z(\zeta) \sim 1/\zeta$.

Substituting this back into the resonance condition and simplifying, one obtains the original dispersion relation of equation 2.16, and the fluid (cold plasma) Theory

holds, provided:

$$\left|\frac{\omega - \omega_{c_{min}}}{k_{||} v_{th_{min}}}\right| >> 1 \tag{2.20}$$

in the case of $|(\omega - \omega_{c_{min}})/k_{||} v_{th_{min}}| \sim 1$, $|(\omega + \omega_{c_{min}})/k_{||} v_{th_{min}}| >> 1$, and $Z(\zeta^{+}_{min})$ can be neglected. For the heated plasma, equation 2.16 becomes:

$$\frac{\omega^2_{p_{Maj}}}{\omega^2 - \omega^2_{c_{Maj}}} + \frac{\omega^2_{p_{min}}}{2\sqrt{2} k_{||} v_{th_{min}} \omega}[Z(\zeta^{-}_{min})] - N^2_{||} = 0 \tag{2.21}$$

The second term of of the equation represents the minority ion response. This is no longer singular as $\omega \rightarrow \omega_{c_{min}}$ and can pass through the singularity at $\zeta = 0$ so there is no resonance. Therefore the fluid theory does not hold for low minority concentrations (figure 2.1)[5].

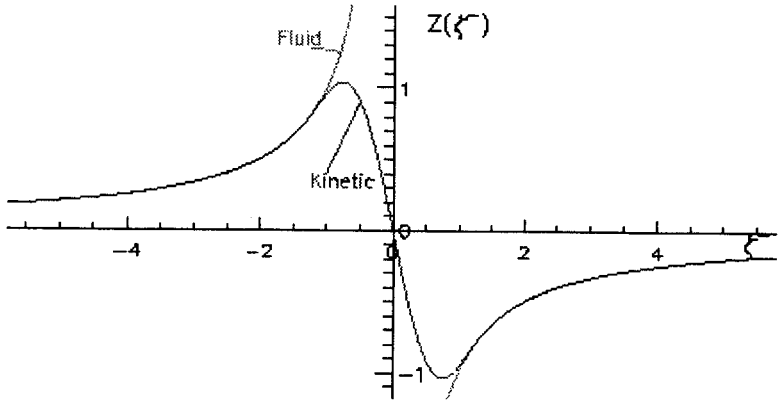

Figure 2.1: Plot of plasma dispersion function (eq. 2.19), showing breakdown of fluid theory at low minority concentrations

This suggests that there is a critical value that marks the transition from the fluid to kinetic regimes, a value which maximizes RF absorption by the minority ions. To find this value, we rearrange eq. 2.21 in terms of $Z(\zeta)$:

$$Z(\zeta^{-}_{min}) = \frac{2}{\eta} \frac{k_{||} v_{th_{min}}}{\omega} \frac{m_{Maj}}{m_{min}} \left[\frac{\alpha^2_m}{1 - \alpha^2_m} + \frac{k_{||} v_{th_{min}}}{\omega^2}\right] \tag{2.22}$$

where:

$$\eta = \frac{n_{min}}{n_{Maj}}$$

and:

$$\alpha_m = \frac{Z_{Maj} m_{min}}{Z_{min} m_{Maj}}$$

Note that the right hand side of eq. 2.22 is now dependent on the minority concentration (η) and not ζ. Figure 2.2 shows a plot of eq. 2.22 for three different minority concentrations. The curve represents the real component of $Z(\zeta^-_{min})$ vs. ζ^-_{min} (eq. 2.19), The right hand side of eq. 2.22 (independent of ζ) for three different minority concentrations is represented by the dashed horizontal lines, with solutions being the intersection of the dashed lines with the curve of eq. 2.19. For values of η less than the critical value (minority regime, upper line) there is no intersection, and therefore no real valued solutions, as far as ω is concerned (any such solutions are complex). Any damping in this regime will occur for other reasons, which are outside the scope of this thesis.

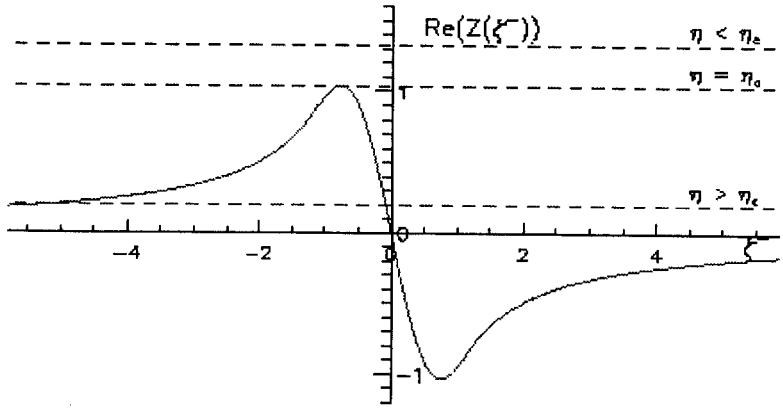

Figure 2.2: Plot of plasma dispersion relation (eq. 2.21). The dashed lines represent three different minority ion concentrations (right hand side of eq. 2.22)

For values of η greater than the critical value (mode conversion regime, lower line), there are two solutions, one for $\zeta < 1$ and $\zeta > 1$. The $\zeta < 1$ solution is not a true resonance as, eq. 2.19 is dominated by the imaginary component and little or no damping occurs. The $\zeta > 1$ solution, or *hybrid* resonance does occur, and damping is proportional to $1/\eta$. At the transition between the two regimes (middle line, tangent to curve) one can see that there is a critical value of η at which RF

damping is maximized.

Since the value of eq. 2.19 is ~ 1, at the critical level, one can now easily solve for the value of $\eta_{critical}$. [6]

$$\eta_{critical} = \frac{n_{min}}{n_{Maj}} = \frac{2k_{||}v_{th_{min}}}{\omega}\frac{m_{Maj}}{m_{min}}\left[\frac{\alpha_m^2}{1-\alpha_m^2} + \frac{k_{||}v_A}{\omega^2}\right] \tag{2.23}$$

where $v_{th_{min}}$ is the minority ion thermal velocity:

$$v_{th_{min}} = \sqrt{\frac{kT_{min}}{m_{min}}}$$

and v_A is the Alfvén velocity:

$$v_A = \frac{B}{(\mu_0\rho)^{1/2}}$$

The critical minority concentration is therefore found to be dependent on the minority ion temperature (kT_{min}), plasma mass density (ρ), and the magnetic field strength (B).[7]

Chapter 3

Experiment

The majority of plasma discharges on C-Mod use a toroidal field of approximately 5.4 T at the location of the plasma magnetic axis. For ICRF auxiliary heated plasmas, hydrogen is used as the minority species which, for this field value, is resonant at 80 MHz. High field shots, where B $\sim$ 8 T, use Helium-3 (^{3}He) as the minority species, since they are also resonant at 80 MHz. The RF system operates at 80 MHz, and provides up to 3 MW of auxiliary power.

The plasma minority concentration, or hydrogen/deuterium (H/D) ratio, is measured by observing the Balmer-α (n=3 $\rightarrow$ n'=2) transitions of each isotope (where n is the principal quantum number, an integer). The resulting emissions occur at the inner and outer edges of the plasma, where excitation and recombination of neutrals takes place. For hydrogen (Z = 1) the energy difference between the two levels is given by:

$$\Delta E = E_g(\frac{1}{n'^2} - \frac{1}{n^2}) = \frac{\mu}{m_e} Z^2 E_0(\frac{1}{2^2} - \frac{1}{3^2}) \tag{3.1}$$

where E_g is the ground state energy of hydrogen and μ is the reduced mass of the electron + nucleus:

$$\mu = \frac{m_e M}{M + m_e}$$

μ/m_e is of order unity for hydrogen. E_0 is the *Rydberg energy unit* [8], given by:

$$E_0 = \frac{e^2}{4\pi\varepsilon_0}\frac{m_e}{2\hbar} \sim 13.6eV$$

The transitional energy $\Delta E_{3\to 2}$ of eq. 3.1 is $\sim$ 1.89 eV, which gives a wavelength, (λ_0), of $\sim$ 656 nm.

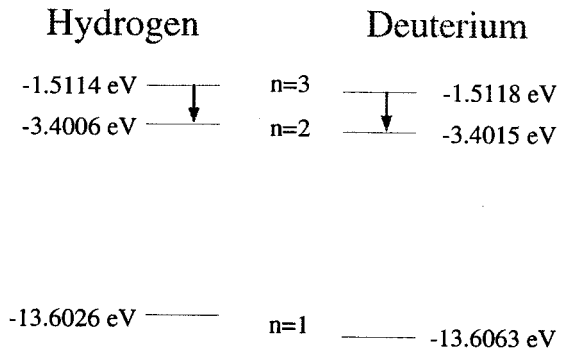

Figure 3.1: Electron energy levels for hydrogen and deuterium. Arrows represent Balmer-α transitions. (not to scale)

The mass of the additional neutron of deuterium will change the value of μ slightly. As a result there is a small but measurable difference in the energy levels between hydrogen and deuterium (figure 3.1), changing the respective wavelengths of the line emission of each ion species. In air at standard temperature and pressure, these values are:

$$\lambda_H = 656.2793\,\text{nm}$$
$$\lambda_D = 656.1032\,\text{nm}$$

and the difference is well within the resolving power of conventional optical spectrometers.

3.1 Hardware

The plasma observation port is located on K-port, $\sim$ 7.5 cm below the midplane of the plasma (figure 3.2). Four fiber optic cables collect the photons emitted from the plasma edge and run beween the diagnostic window on K-port and the spectrometer input. Three of these cables are currently used with separate fixed polarizing filters for each.

3.1.1 Spectrometer

The spectrometer is a modified 1 meter (f=1000 mm) Ebert double-slit monochromator. A 1200 mm^{-1} (d=833 nm) grating is located at the focus of the spherical mirror. The exit slit is bypassed by a 45° plane mirror which directs the image to the optical detector mounted to the side (figure 3.3). The detector is positioned in the focusing plane, which is an optical distance of f (1000 mm) from the spherical mirror.

Dispersion

The entrance slit is located at a distance d (76.2 mm) from the spherical mirror axis of symmetry. The angle ϕ between this axis and the ray traveling from the entrance slit to the mirror is:

$$\phi = tan^{-1}\frac{d}{f} = tan^{-1}\frac{76.2mm}{1000mm} = tan^{-1}0.0762 = 4.35°$$

θ is the angle between the grating normal and the symmetry axis. The *reciprocal dispersion relation* in second order (m=2):

$$\frac{\partial\lambda}{f\partial\theta} = \frac{d}{mf}\cos\theta\cos\phi = \frac{833\,\text{nm}}{(2)(1000\,\text{mm})}cos(308°)cos(4.35°) \qquad (3.2)$$

yields a net dispersion of 0.256 nm/mm at the focus.[9]

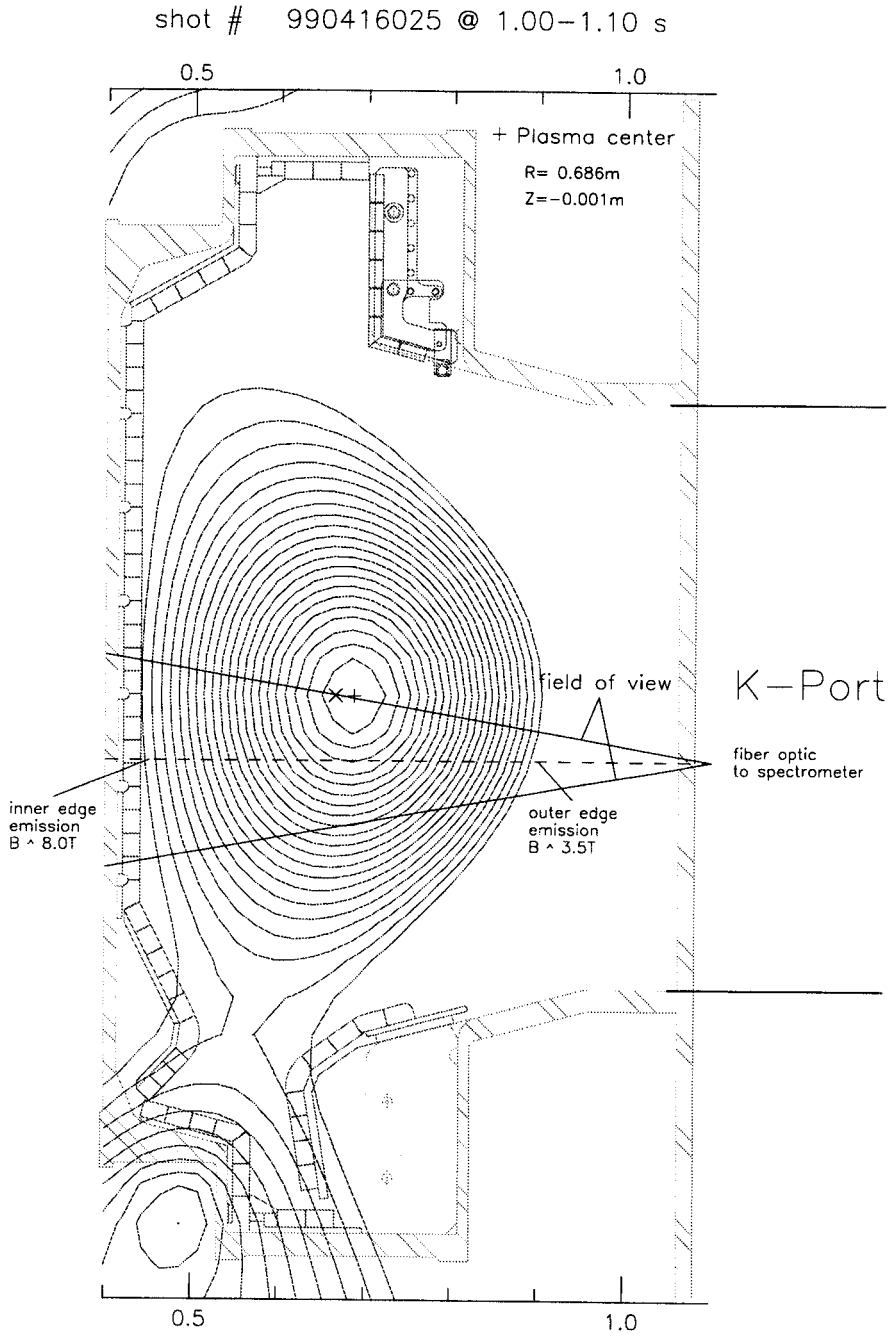

Figure 3.2: Poloidal cross section of plasma, showing fiber optic location in K-Port. B field values are given as 5.4 T on axis (R=0.67 m)

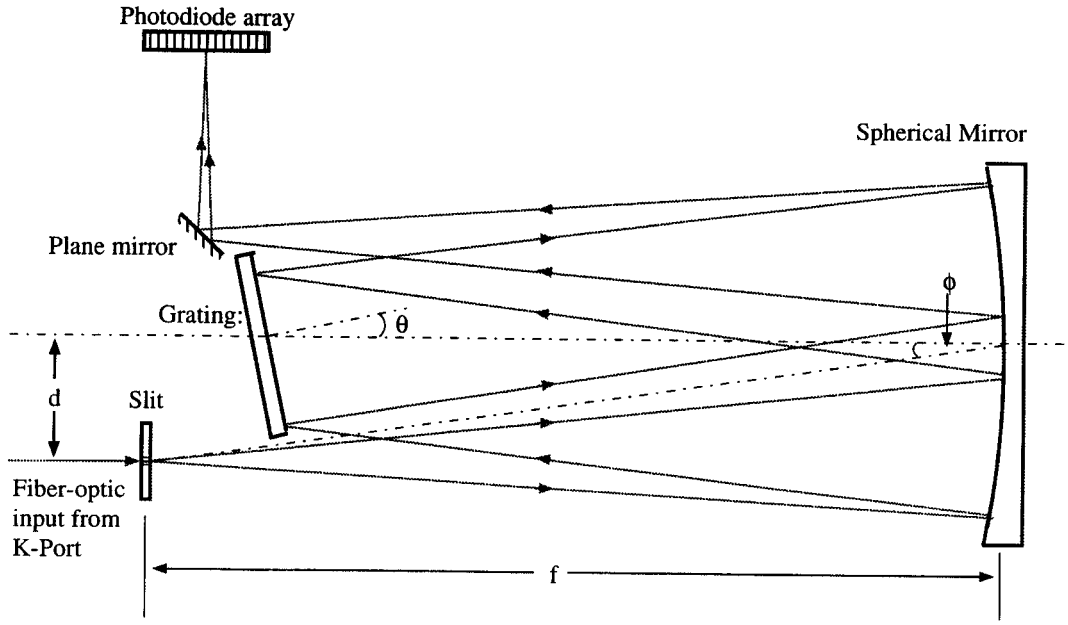

Figure 3.3: Modified Ebert spectrometer layout

Resolution

The entrance slit is adjustable, but in this case it is opened completely. The effective width, w_s, is then equal to the width of the fiber optic cable, in this case, 100 μm. This will produce a gaussian distributed line (Λ) at the focus.The Full Width of this line at Half the Maximum value, or FWHM, is found from the dispersion relation of equation 3.2:

$$\Lambda_{FWHM} = w_s \frac{\partial \lambda}{f \partial \theta} = (0.1mm)(0.256nm/mm) = 0.0255nm \tag{3.3}$$

We have established as our criterion that to resolve two identical overlapping gaussian peaks of height, f_0, separated by a distance $\Delta\lambda$ (valid for $\Delta\lambda << \lambda_0$); the sum of the curves midway between the peaks must be less than $1/\sqrt{2}$ of the maximum value A (figure 3.4). For simplicity, we will assume that $A \sim f_0$. The peaks can therefore be no closer than twice the half width (or the full width) at

$1/2\sqrt{2}$ if they are to be resolved [10].

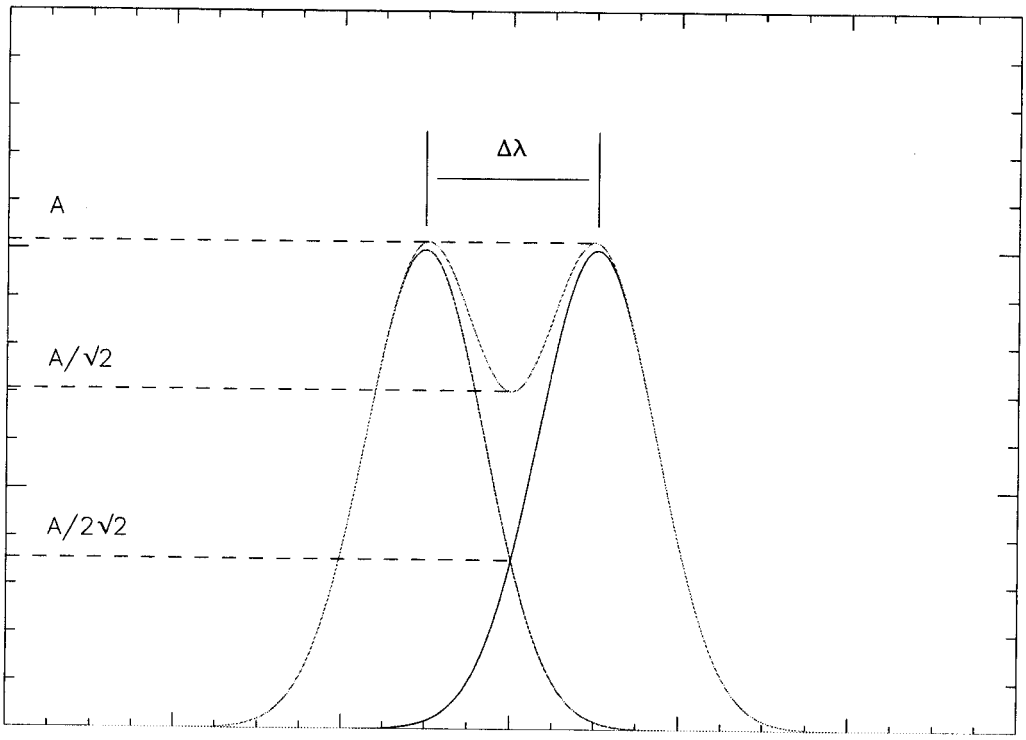

Figure 3.4: Criterion for spectral line resolution

For an effective slit width of 100 μm, the minimum separation $\Delta\lambda$ that can be resolved by the spectrometer is:

$$\Delta\lambda = \Lambda_{FWHM}\frac{(\text{Full Width at } 0.3536)}{(\text{Full Width at } 0.5000)} = 0.0225nm\frac{1.0917}{0.8326} = 0.0334nm \qquad (3.4)$$

3.1.2 Detector

A Reticon 64 element photodiode array is used as the optical detector. The detector array is 2.5 mm high by 3.2 mm long and has a density of 20 diodes/mm (64 elements $\sim$ 0.05 mm wide each). This gives, using the dispersion relation from equation 3.2, an overall spectral dispersion of $\sim$ 0.0112 nm/pixel, and a spectral range of $\sim$ 0.72 nm.

The detector is mounted on a three-way translation stage to allow movement $\sim$ 5 cm in the x,y and z directions. In addition there is a three-axis rotational platform

mounted on the stage which allows $\pm 1.5°$ rotation about the horizontal (x), vertical (y) and longitudinal (z) axes (angles γ, β, and α, respectively), for a total of six degrees of freedom (figure 3.5).

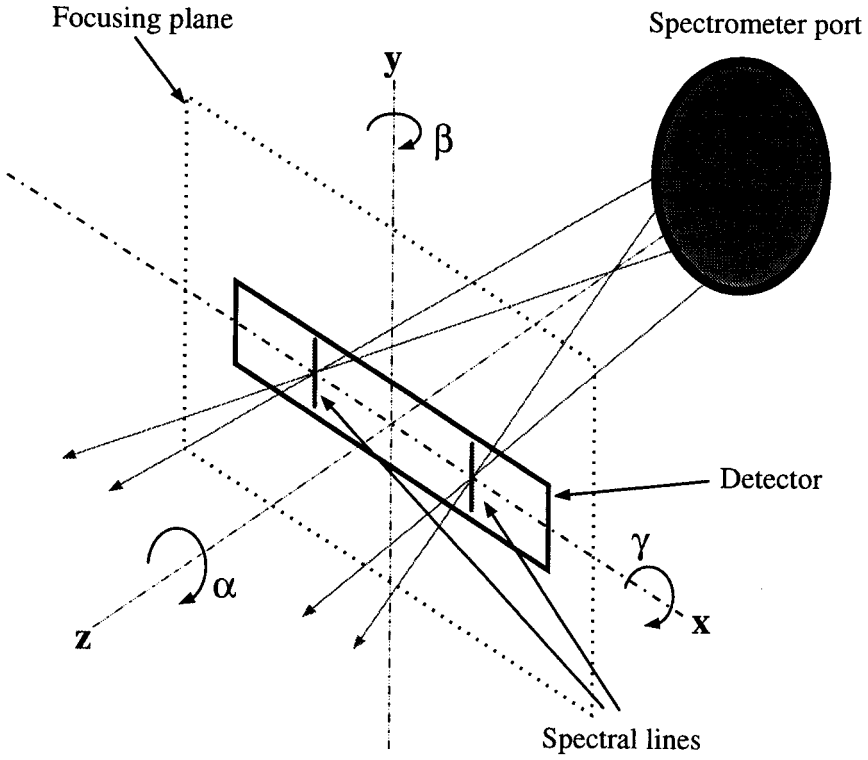

Figure 3.5: Alignment of optical detector

The signal is typically digitized at a line rate of 20 Hz. This gives an integration time of 50 ms. The signal from the array is integrated and averaged for 50 ms, and read out for the last 0.64 ms of the cycle. The signal from each element is stored in a 12-bit register, giving a range of 4096 counts per channel. There are two digitizer channels in use. The first receives the raw signal, the second is amplified to 10x prior to digitization. One can select between the two, in order to provide a greater overall dynamic range.

3.1.3 Polarizing Filters

Spin-orbit interactions between the hydrogen electrons and the plasma magnetic field (most notably the Zeeman Effect, figure 3.6) pose an interesting challenge to resolving the isotopic signals. The strong magnetic fields ($\sim$ 5 T) in use will produce a significant wavelength shift of the spectral lines relative to their separation ($\Delta\lambda_{H-D}$) The wavelength shift, $\delta\lambda$, is proportional to the frequency shift $\delta\nu$, given by:

$$\delta\nu = m_\ell \frac{eB}{4\pi m_e} = c\left(\frac{1}{\lambda_0} - \frac{1}{\lambda_0 + \delta\lambda}\right) = c\frac{\delta\lambda}{\lambda_0(\lambda_0 + \delta\lambda)} \sim \frac{c}{\lambda_0^2}\delta\lambda \tag{3.5}$$

where ℓ is the angular momentum quantum number, an integer ranging from 0 to (n-1). m_ℓ is the angular magnetic quantum number, also an integer, ranging from $-\ell$ to $+\ell$. Quantum selection rules dictate that $\Delta\ell = \pm 1$, and, in the case of Balmer-α transitions, Δm_ℓ is -1, 0, or +1.

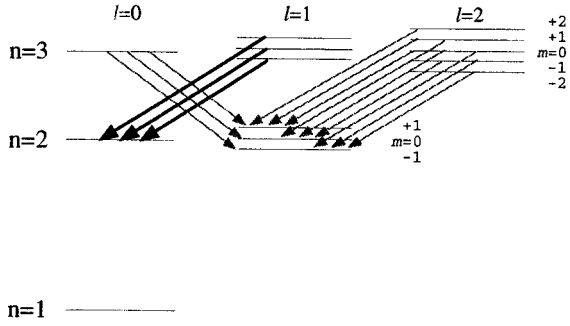

Figure 3.6: Zeeman splitting of Balmer-α lines. In addition to the principal quantum transition (Δn), there is a splitting of each level associated with the change in angular magnetic quantum number, Δm_ℓ

Therefore, the spectral lines of interest are split into three components. There are two shifted, or $\sigma\pm$ lines, one on either side of an unshifted, or π line. The component

wavelength shifts are:

$$\delta\lambda = \left\{ \begin{array}{lll} \pm\frac{\delta\nu\lambda_0^2}{c}. & \Delta m_\ell = \pm 1 & (\sigma \pm \ lines) \\ 0, & \Delta m_\ell = 0 & (\pi \ line) \end{array} \right\} \tag{3.6}$$

or about $\pm$ 0.02 nm/Tesla for the observed wavelength.[11] A typical field strength of 5.4 T produces a splitting of 0.108 nm, which is of the same order as $\Delta\lambda_{H-D}$.

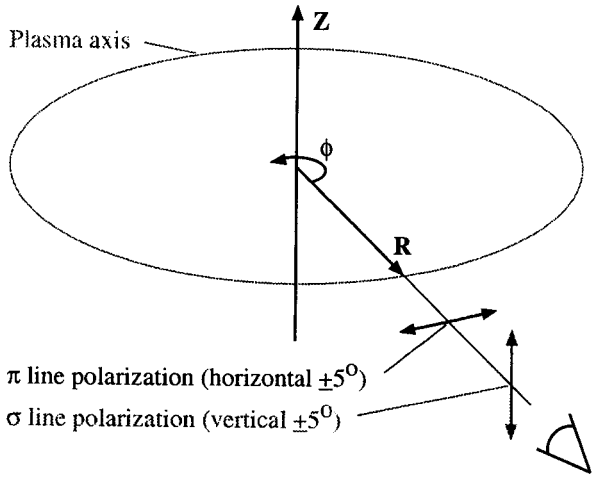

Figure 3.7: Polarization of π and σ lines with respect to machine coordinates

When viewed perpendicular to the magnetic field (**B**), the shifted ($\sigma\pm$, $\Delta m_\ell \pm 1$) lines are polarized in the direction perpendicular to both **B**, and to the emission direction. The unshifted (π, $\Delta m_\ell = 0$) lines are polarized parallel to **B** (figure 3.7). Two of the fiber-optic cables are equipped with polarizing filters, one parallel to $\mathbf{B}_\phi$, the other perpendicular to $\mathbf{B}_\phi$. This arrangement has the advantage of allowing one to select the desired polarization on a shot-by-shot basis: horizontal ($||$ to **B**, for π lines), vertical ($\perp$ to **B**, for $\sigma\pm$ lines), or no polarization. This can be done by switching fibers at the input of the spectrometer, eliminating the need to enter the tokamak test cell during the run period.

3.2 Calibration

3.2.1 Source

A deuterium gas discharge tube is used to calibrate the spectrometer. The lamp produces a strong optical peak at 656.10 nm. A smaller peak at 656.28 nm due to hydrogen contamination is present and is, in fact, desired. This allows the two spectral lines of interest to be accurately located for purposes of focusing and alignment (figure 3.8).

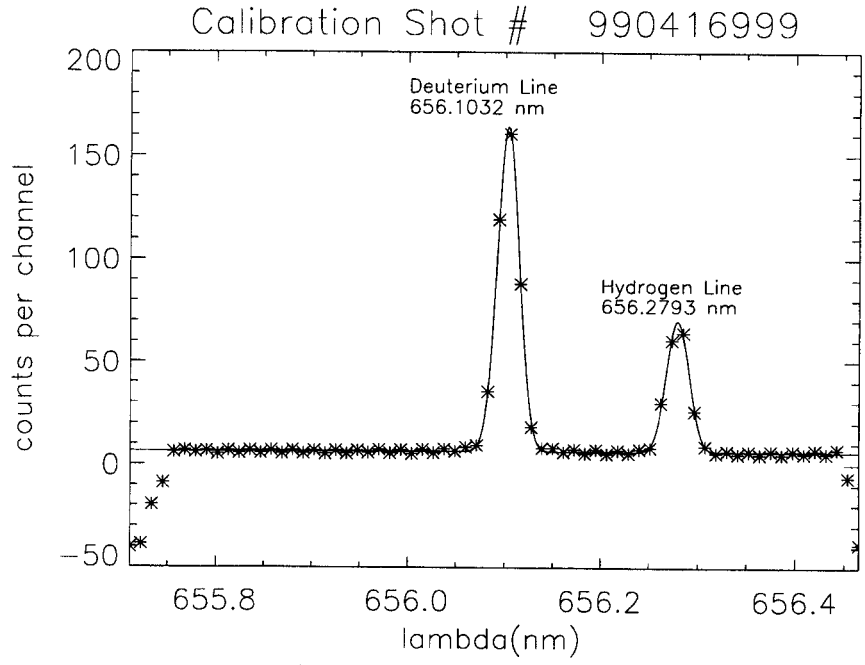

Figure 3.8: Deuterium lamp calibration, showing deuterium and hydrogen lines

3.2.2 Alignment

Light from the D_2 lamp is directed to the spectrometer via a short fiber optic cable connected in place of the fiber from K-port. The clock pulse is switched to the ungated output for continuous triggering. The output from the detector is observed by oscilloscope, while the six parameters of the detector are adjusted.

The detector is first positioned in z, moving it along the z axis until line width is minimized. This establishes its general position in the focusing plane (figure 3.5).

Second, the detector is rotated about the z axis (α), also seeking minimum peak width, to ensure that the spectral lines are aligned with the boundaries of the detector elements. More importantly, this establishes that the photodiode array is aligned squarely along the dispersion direction ($||$ to the x axis).

Next, the detector is positioned in y, to ensure that the detector intercepts the entire beam.

Fourth, the detector is moved along x, to refine the peak of interest location on the array. (This is established by setting the grating angle θ). Currently the detector is positioned with the deuterium peak in the center of the array (figure 3.8).

Finally, rotation about x and y (γ and β) are adjusted, further refining the focus. The small vertical size of the detector makes the focus less sensitive to these parameters, and therefore these last two adjustments are not as critical as the first four.

3.2.3 Test Shot

Prior to the start of a run, the D_2 lamp is connected to the spectrometer and a test exposure is taken (figure 3.8). The position of each peak is manually selected via a cursor and is used to establish the wavelength values along the horizontal (X) axis. The X axis is 64 points which correspond to the 64 pixel elements in the detector array. The two spectral lines are fitted by gradient-expansion to produce a non-linear least-squares fit based on the sum of two gaussian distribution curves:

$$F(\lambda) = b_o + \sum_i f_{o_i} e^{-(\frac{\lambda - \lambda_i}{\sigma w_i})^2} \tag{3.7}$$

where f_{o_i} is the maximum value of each spectral line, and λ_i is the Balmer-α wavelength for each isotope, and b_o is the background intensity. The manually selected

postion of each peak is matched to each λ_i value to determine the wavelength in terms of X. The trial function of equation 3.7 is supplied as an input. The width of each spectral line, represented by σ_{w_i}, is estimated in the trial function, and a calculated value is returned by the algorithm for the actual fitted curve. The curvefit algorithm is embedded in a calibration code which returns three primary values: offset, slope, and width.The *offset* parameter represents the first wavelength value on the x axis. *Slope* is the dispersion of wavelength per pixel. *Width* is the spectral line half width at 1/e (averaged between the two peaks).

From a test shot taken on April 16, 1999 (figure 3.8), the values returned from the calibration code are:

Offset: 655.71 nm
Slope: 0.0112 nm/pixel
Width: 1.4255 pixels

Applying the resolution criteria gives the *instrument spectral resolution*, or σ_r:

$$\begin{aligned}\sigma_r &= (\text{FW at 1/e in pixels})(\text{disp. per pixel})\frac{(\text{FW at 0.3536})}{(\text{FW at 1/e})} \\ &= 2(Width)(slope)1.0917 = 0.0350nm\end{aligned} \tag{3.8}$$

which is very close to the theoretical resolution limit estimated by equation 3.4.

Currently, variations are small enough that a calibration test shot need only be taken once per week. A recent change to the ratio calculation program is to use the deuterium peak of a plasma shot as a trial function, to establish the position of the deuterium line. This makes periodic calibration shots necessary only to verify detector alignment.

Since only the relative spectral peak height between the two species is needed, it is not necessary to convert the number of counts per channel to absolute intensity.

3.2.4 Analysis of Uncertainty and Error

Due to the rotational transform associated with the plasma current in the tokamak, the spectral line polarizations are tilted of order $\pm 5°$ with respect to the horizontal and vertical, so a small amount of the unwanted signal passes through the filter in each case. Further, due to the 1/R dependence of $\mathbf{B}_\phi$, there is a difference of nearly a factor of 2 in Zeeman splitting between the inner and outer edges of the plasma.

The preferred method in viewing the Balmer-α is to use horizontal polarization as opposed to vertical as there is greater uncertainty in observing the $\sigma\pm$ than with the π lines. Orienting the polarizer in the horizontal ($\hat{\phi}$) direction can filter out nearly 95% of the $\sigma\pm$ emission.

3.3 Signal Observation and Analysis

3.3.1 Curve Fits

Information from the spectrometer may be extracted by applying a curve fit similar to the method used in the calibration shot (eq. 3.7). For an actual shot, the individual spectral lines are represented by gaussian curves of the form:

$$f_{ij}(\lambda) = f_{o_{ij}} e^{-(\frac{\lambda-\lambda_i+\delta\lambda_j}{\sigma_{w_{ij}}})^2} \tag{3.9}$$

where, as before, f_o is the individual peak height, and λ_i is the wavelength associated with each ion species. In addition there is $\delta\lambda_j$, the Zeeman splitting shift in wavelength (zero for π lines) for the inner and outer edges of the plasma, and $\sigma_{w_{ij}}$ is the average peak half-width at (1/e) for each spectral line, primarily due to doppler broadening[12]. For a two species plasma, there are four shifted lines ($\sigma^{\pm}_{inner}$ and $\sigma^{\pm}_{outer}$) for both species, plus the two unshifted π lines for a total of ten curves. The

resultant fitted curve is represented by the sum of the curves:

$$F(\lambda) = b_0 + \sum_i \sum_j f_{0_{ij}} e^{-(\frac{\lambda-\lambda_i+\delta\lambda_j}{\sigma w_{ij}})^2} \tag{3.10}$$

H/D Ratio by Curve Fit

Once a satisfactory fit is established, the H/D Ratio η may be calculated from the relative intensity of each isotope line. For the horizontally polarized view, this is accomplished by comparing the area under the π line curve of each species:

$$\eta = \frac{\int f(\lambda_H)d\lambda}{\int f(\lambda_D)d\lambda} = \frac{\int f_H e^{-(\frac{\lambda-\lambda_H}{\sigma w_{H_\pi}})^2} d\lambda}{\int f_D e^{-(\frac{\lambda-\lambda_D}{\sigma w_{D_\pi}})^2} d\lambda} \tag{3.11}$$

Likewise, the vertically polarized views use the area under the $\sigma+$ curve of each for comparison:

$$\eta = \frac{\int f(\lambda_H)d\lambda}{\int f(\lambda_D)d\lambda} = \frac{\int f_H e^{-(\frac{\lambda-\lambda_H d\lambda+\delta\lambda}{\sigma w_{H_\sigma}})^2} d\lambda}{\int f_D e^{-(\frac{\lambda-\lambda_D d\lambda+\delta\lambda}{\sigma w_{D_\sigma}})^2} d\lambda} \tag{3.12}$$

with $\delta\lambda$ being the wavelength shift produced by the Zeeman Effect (eq. 3.6). The inner edge splitting value ($\delta\lambda_{inner}$) is used, due to the uncertainty of splitting associated with the outer edge. With integration and the application of some algebra, equations 3.11 and 3.12 simplify to:

$$\eta = \frac{f_H \sigma_{w_H}}{f_D \sigma_{w_D}} \tag{3.13}$$

Where f and σ are the heights and widths of the particular curves being compared.

Ion Temperature at Plasma edge

A satisfactory curve fit can also be used to determine the kinetic temperature of the emitting neutrals at the plasma edge [13]. Due to thermal motion, the spectral lines will be doppler broadened. One may assume a Maxwellian velocity distribution

function, $f(v)$, for the plasma:

$$f(v) = (\frac{m}{2\pi kT})^{3/2} e^{-\frac{v^2}{v_{th}^2}} \tag{3.14}$$

where the velocity is represented by:

$$v = \sqrt{v_x^2 + v_y^2 + v_z^2}$$

and the thermal velocity is:

$$v_{th} = \sqrt{\frac{2kT}{m}}$$

As with the Gaussian distribution, the width of the curve of eq. 3.14 is represented by the denominator of the exponent. This is v_{th}, which is proportional to the square root of the kinetic temperature, kT. Therefore, the width of the thermal distribution curve is proportional to $\sqrt{kT/m}$. With some algebra, the ion temperature at the plasma edge can be calculated by:

$$kT(\text{keV}) = m_i(\text{amu}) \frac{\sigma_F^2 - \sigma_r^2}{\lambda_i^2(\text{nm})} (7.75 \times 10^{-5})^{-1} \tag{3.15}$$

where σ_r is the instrumental resolution, determined in the calibration shot. σ_F is the measured FWHM of the spectral line, given by:

$$\sigma_F = \text{FWHM} = 2\sqrt{\ln 2}\sigma_w$$

with σ_w being the average half-width at (1/e) of the spectral line (from eq. 3.9)[14].

Curvefit Results

Figure 3.9 shows a fitted curve obtained from shot 990305016. The polarization is horizontal. The raw data points are the light blue stars while the solid magenta line represents the fitted curve. The colored lines represent the individual gaussian curves

for each spectral line described by eq. 3.9. (The offset is omitted for clarity in this case). The hydrogen $\sigma\pm$ lines were not visible in this shot and are not labeled. Since the main hydrogen π line is of low intensity it is reasonable to assume that the lines were simply too dim to be detectable in this shot. This particular fit would appear to be a reasonable representation of isotopic conditions in the plasma.

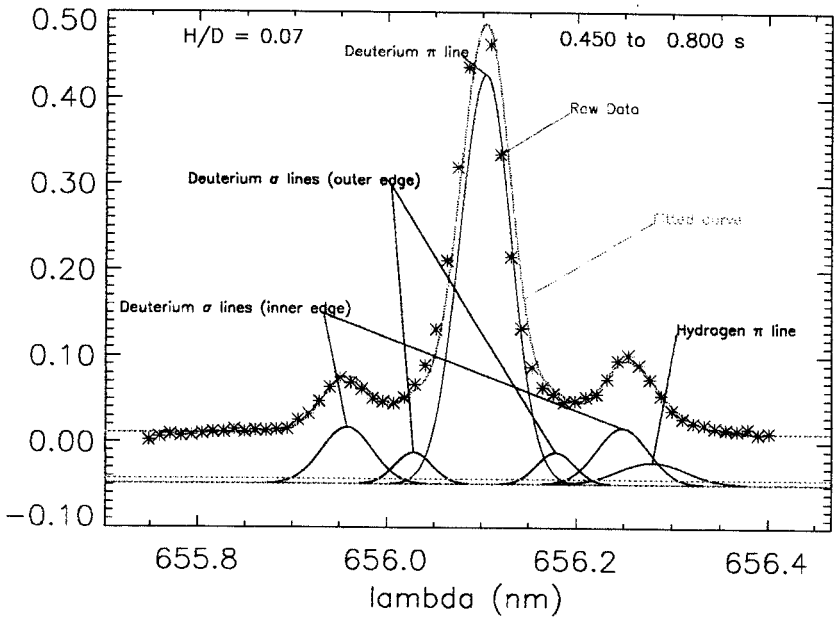

Figure 3.9: Fitted curve for shot 990305016. (Hydrogen $\sigma\pm$ lines not visible)

Due to changing conditions in the plasma, it is not practical to use this method for time averaging longer than ~ 0.25 s, as this will produce fits that do not reflect actual physical conditions in the plasma (figure 3.10). The curves representing the Deuterium σ lines (dark blue) are much too broad to be accounted for by 1/R variation of $\mathbf{B}_\phi$, so this is a poor fit.

Conversely, too short of a time averaging interval will make the raw data points more difficult to fit as there is less smoothing of the overall spectrum. Figure 3.11 shows a somewhat reasonable curve fit, but there is a strong difference in inner and outer edge intensity, This also does not appear to represent actual plasma conditions, at least as far as the $\sigma\pm$ lines are concerned. On the other hand, the relative ratios

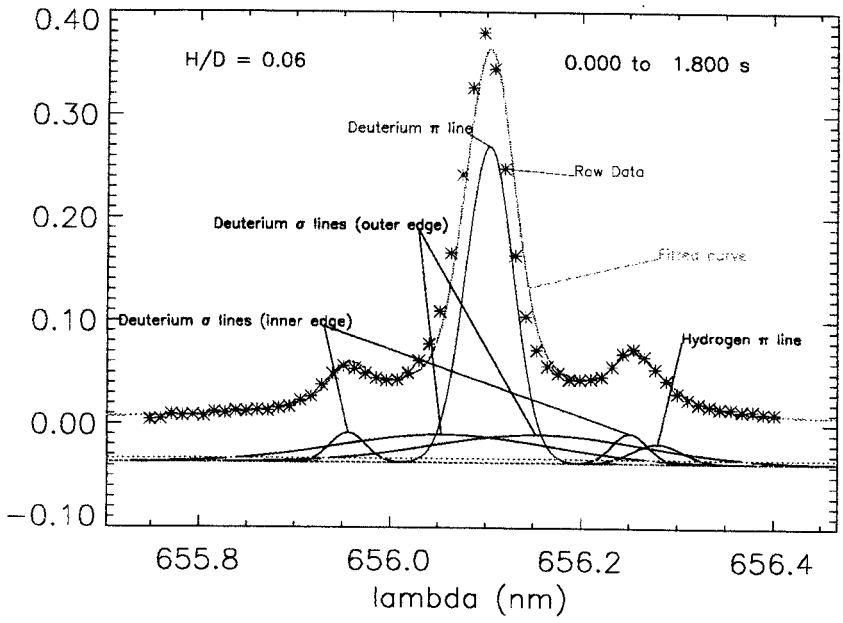

Figure 3.10: Fitted curve for 990305016 taken over the entire duration of shot. The outer edge D $\sigma\pm$ line curves are too broad to be representative of the conditions in the plasma

of area under the π curves does reflect the relative deuterium amount shown in the overall spectrum.

Figures 3.12 and 3.13 show fitted curves for vertical polarization and no polarization, respectively. The same colors are used to designate the individual curves as in figure 3.9. The hydrogen $\sigma\pm$ inner edge (high field, greater splitting) emission lines are now represented by orange curves on the vertical polarizer view. There are no $\sigma\pm$ emission lines represented from the outer edge in either view.

Inspection of figure 3.12 (shot 990202021, using vertical polarizing filters) shows that the spectrum is clearly dominated by deuterium emission. However the inner edge hydrogen $\sigma\pm$ curves (orange) are much larger than the inner edge deuterium $\sigma\pm$ (green) lines. As a result, the H/D ratio is given as 6.40, when inspection of the overall spectrum suggests otherwise. Clearly, this is a poor fit.

In figure 3.13 (shot 990205021, using no polarizing filters) there are no hydrogen $\sigma\pm$ lines represented in the curve fit, while the deuterium $\sigma\pm$ lines figure prominently.

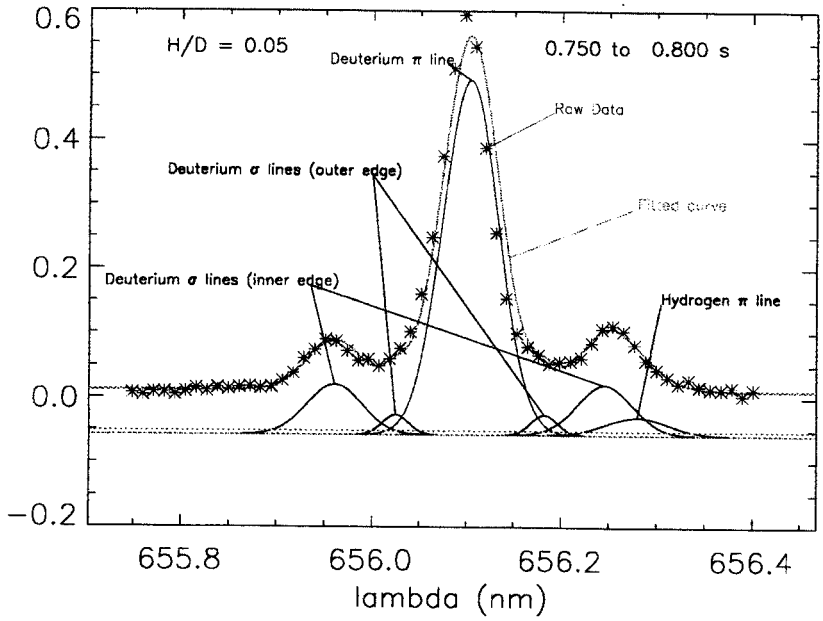

Figure 3.11: Fitted curve for shot 990305016 (single integration, 50 ms time interval)

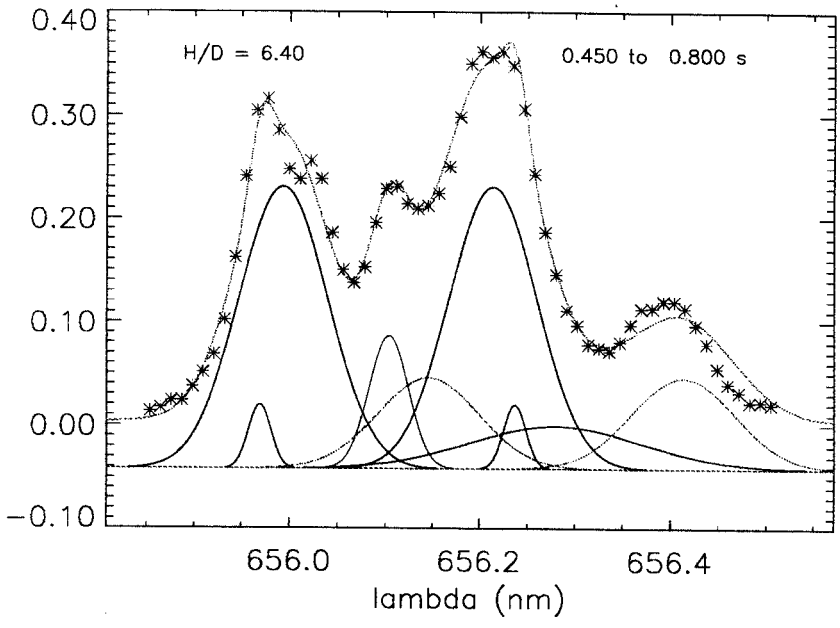

Figure 3.12: Fitted curve for shot 990202021 (vertical polarization)

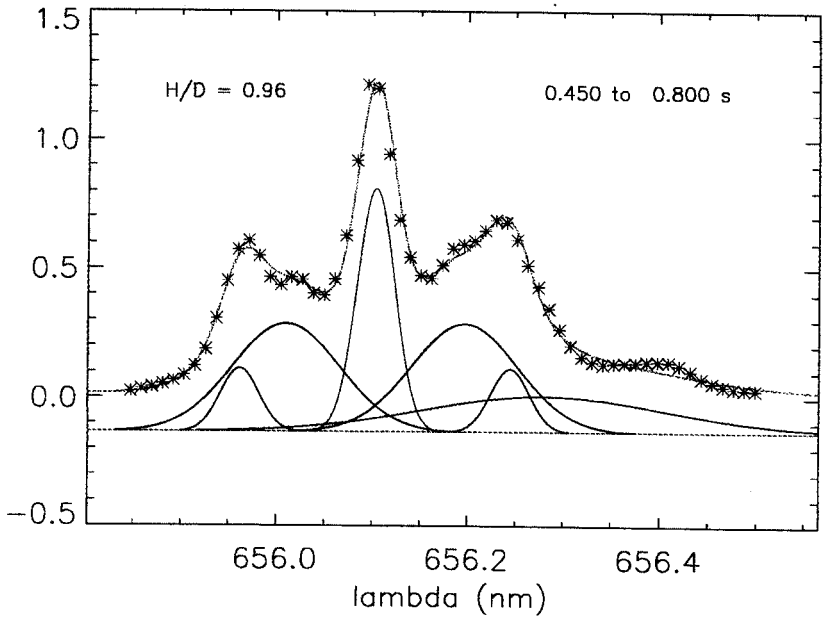

Figure 3.13: Fitted curve for shot 990205021 (no polarizing filters)

This is not entirely unreasonable, as this spectrum is also dominated by deuterium emission. There is a peak in the raw data at 656.4 nm which suggests hydrogen σ emission line, but this is not fitted by the routine. A more serious problem, however, is the extreme width of the hydrogen π line curve fit. This makes the area under this curve nearly equal to the area under the deuterium curve. The calculated H/D ratio is nearly unity. Since this shot also appears to be dominated by deuterium, this would again seem to be a false representation of conditions. Other attempts at curve fitting of vertically polarized or unpolarized views have been equally unsuccessful.

In summary, the best results of the curve fit routine are obtained by looking at 4-6 frames (0.15-0.25 s at the 20 Hz digitization rate) of a shot using the horizontal polarizing filter.

3.3.2 H/D Ratio by Weighted Average

While the curve fit routine may be used to determine the minority concentration for a particular time in the shot, it is too cumbersome for use in tracking the evolution

of the ratio over the course of a shot. Also the curve fit method is not reliable when applied to vertically polarized or unpolarized exposures. A simpler way to accomplish this is to calculate the centroid of the spectral pattern by means of a weighted average:

$$\text{Centroid} = C_g = \sum_{i=1}^{64} \frac{\lambda_i(I_i)}{(I_i)} \tag{3.16}$$

Where I_i is the intensity level above the background I_b.

$$I_i = I_{i_{raw}} - I_b$$

I_b is determined from the average intensities near the two ends of the detector, away from the spectral line emission.

Once the centroid C_g is calculated, the isotopic ratio, η, is determined from the position of C_g relative to the wavelengths of the respective species:

$$\eta = \frac{C_g - \lambda_D}{\lambda_H - C_g} \tag{3.17}$$

which is zero for $n_H = 0$, and one for $n_H = n_D$. The calculation is quick and can be calculated for each individual integration cycle. In this manner, the H/D Ratio can be calculated at 0.05 s intervals (or smaller time intervals at higher digitization rates) [15]. This allows accurate measurement of rapid changes in the ratio over the course of the shot.

Time Average of Ratios

It is sometimes necessary to calculate an average ratio over a specific region of interest (for instance, the time during an RF pulse). The average is simply the sum of values of η at each integration cycle divided by the number of cycles:

$$\overline{\eta} = \frac{1}{(n_2 - n_1 + 1)} \sum_{n_1}^{n_2} \eta_n \tag{3.18}$$

Such averages are often useful in tracking the evolution of the H/D ratio over the course of a shot, run, or several days.

Centroid results

Figure 3.14 shows the ratio calculated by wieghted average (equations 3.16 and 3.17), for the vertically polarized view of shot 990202021. The dashed box indicates the time region examined by the curvefit of plot 3.12. The average H/D ratio during this time is ~ 0.305 Inspection of the raw spectral data of this graph suggests a H/D ratio of roughly 1/3. The ratio calculated via weighted average during this time interval appears to be reasonable.

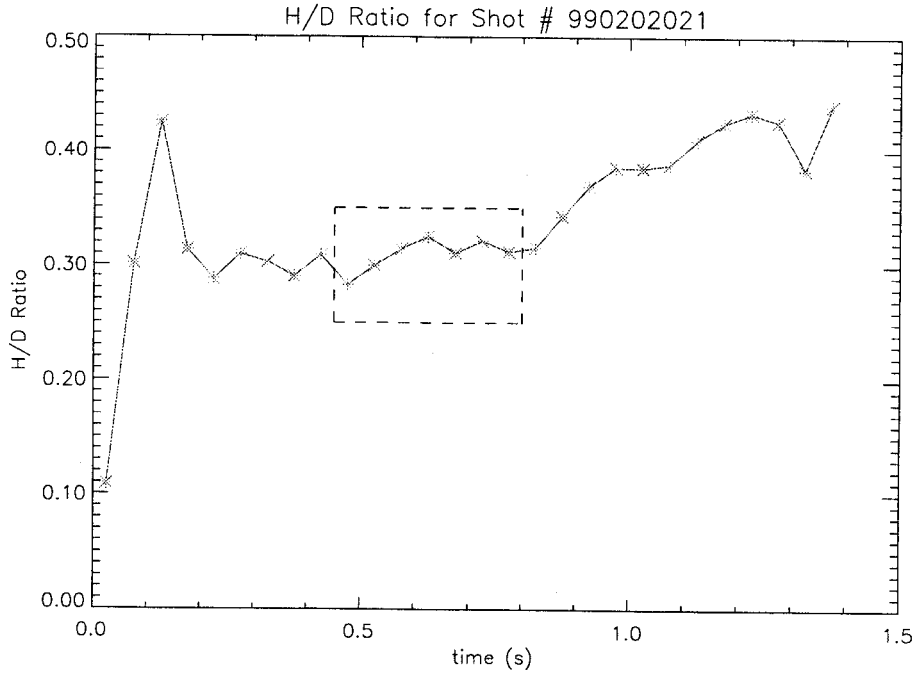

Figure 3.14: H/D ratio for shot 990202021. Dashed lines indicate region examined by curve fit (figure 3.12)

Similarly, inspection of the unpolarized view (figure 3.13) would suggest an H/D ratio of 0.1-0.2. Equations 3.16 and 3.17 give an average ratio of 0.18, which would agree with the raw data. The weighted average method therefore appears to be

sufficiently robust to work well regardless of the polarization filter used. Nevertheless, in standard operation, the horizontal polarization is used.

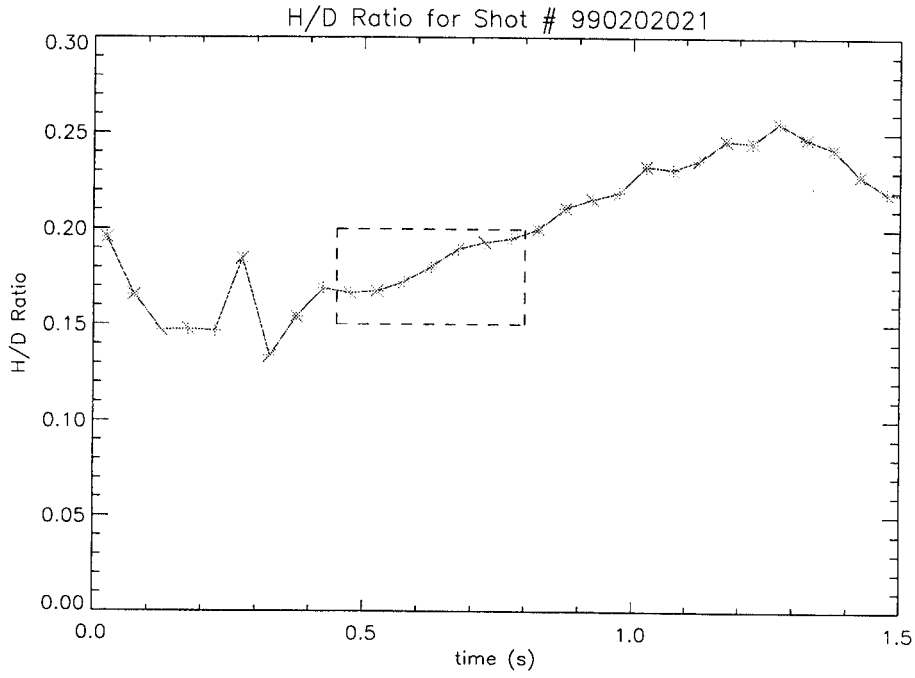

Figure 3.15: H/D ratio for shot 990205021. Dashed lines indicate region examined by curve fit (figure 3.13)

Chapter 4

Observations and Experimental Results

4.1 Observed Trends in H/D Ratio

4.1.1 Evolution of Ratio over Course of Shot

Figure 4.1 shows a shot (# 990205025) from early in the first run campaign of 1999. There is a slow increase of the H/D ratio followed by a rapid rise at 1.0 s, coinciding with the start of the RF pulse. Since this is shortly after pumping of the vessel, following a long vent with extensive personnel access, the increase is likely due to water vapor being emitted from the RF antennas and vessel walls. A later shot, # 990303018, following treatment of the inner vessel with diborane (boronization) in March, shows no significant increase during the RF pulse (fig. 4.2).

A later shot in the February run campaign which achieved enhanced confinement, or H mode [16], is shown in figure 4.3. The ratio remains fairly constant during the RF pulse, increasing only at the end of the pulse.

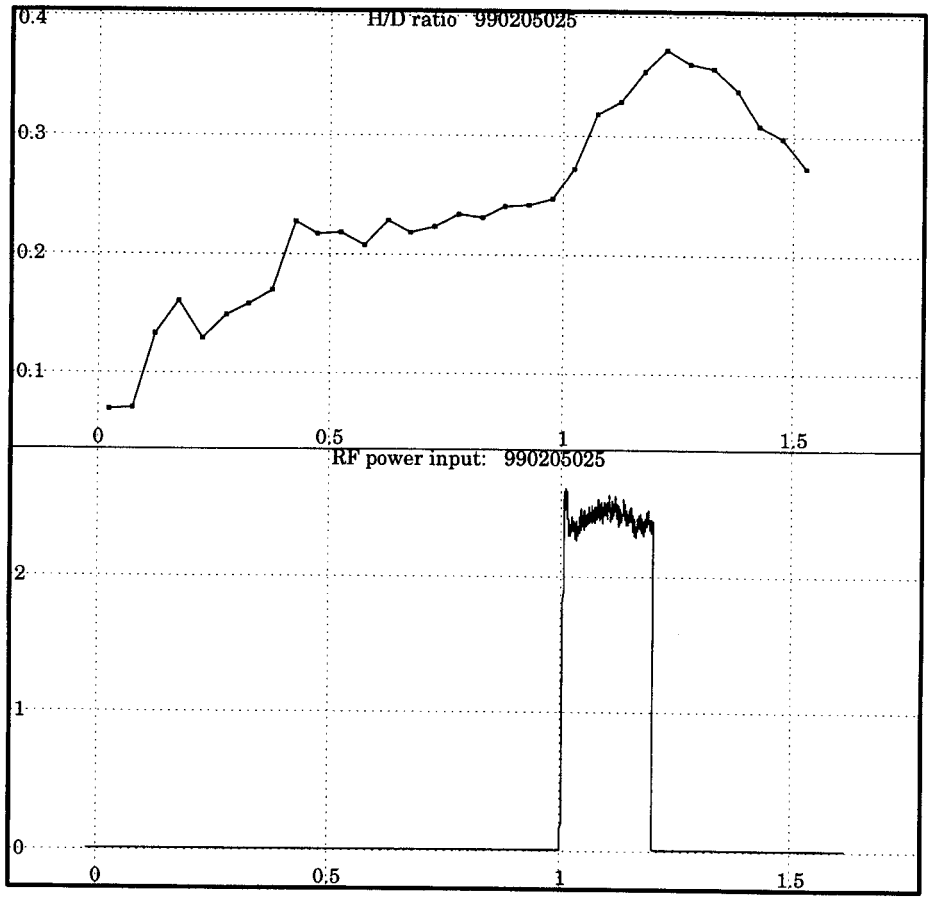

Figure 4.1: Time evolution of H/D ratio for shot, showing sharp rise during the RF Pulse

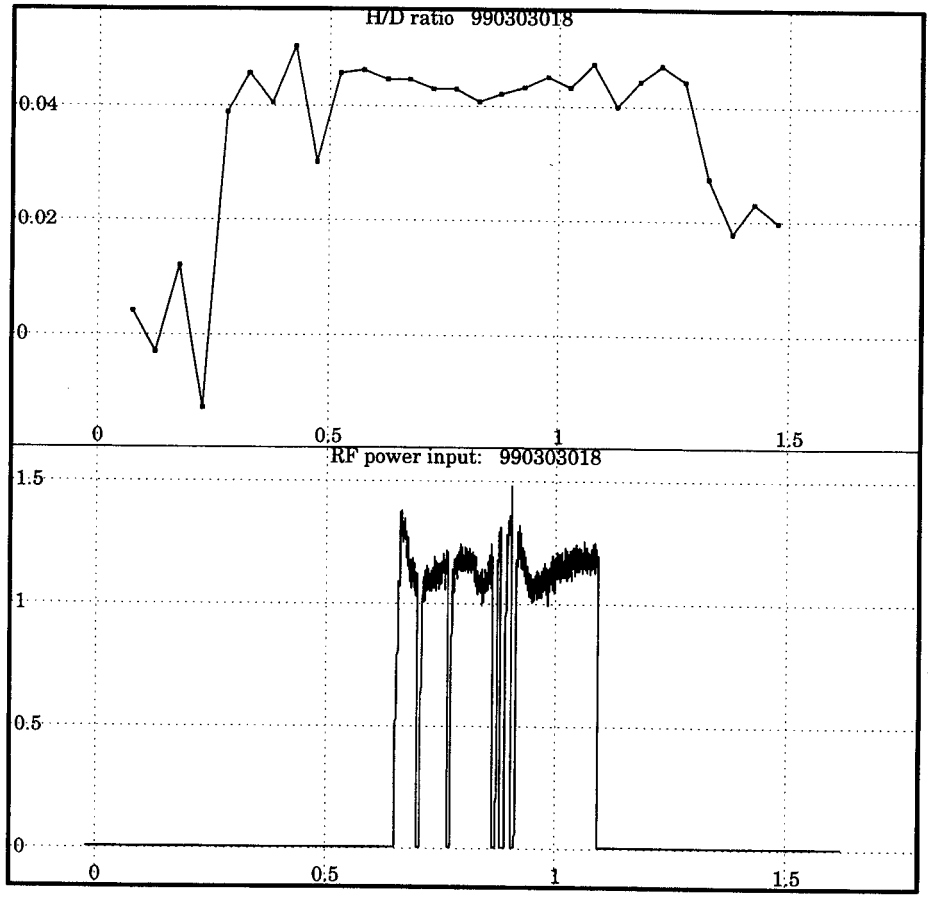

Figure 4.2: Time evolution of H/D ratio for shot 990303018, post boronization, showing little change during the RF Pulse

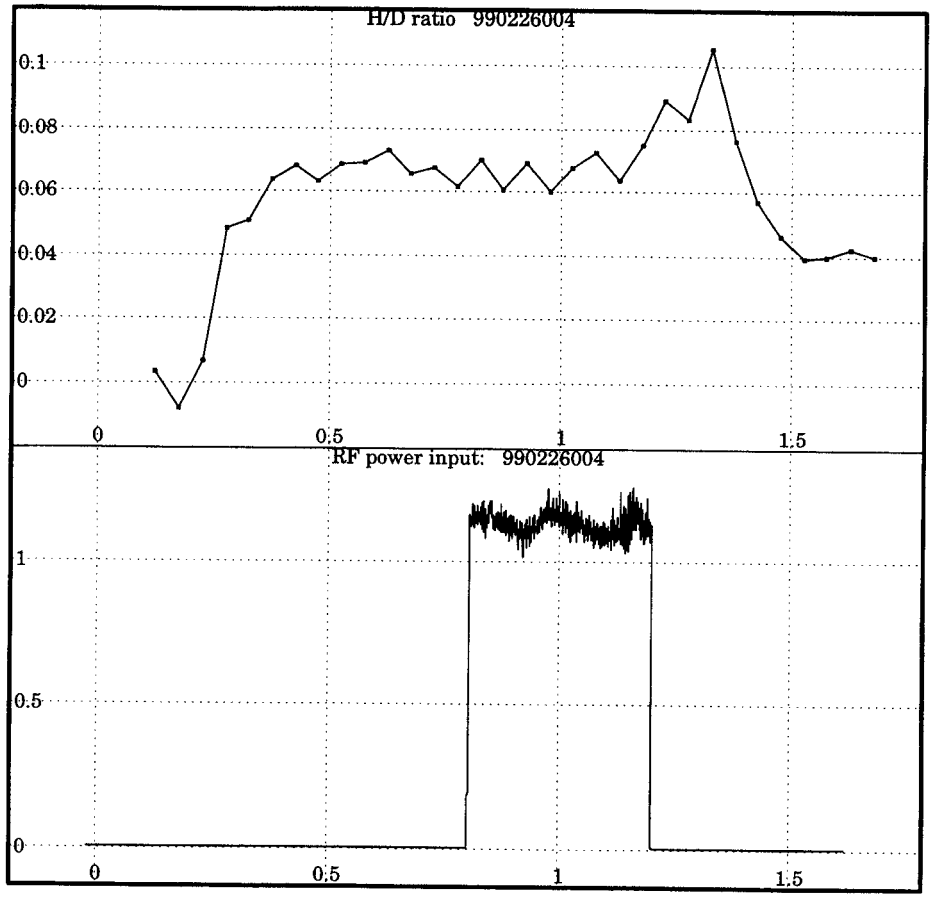

Figure 4.3: Time evolution of H/D ratio for shot 990226004, H-mode, shows little change in ratio during the RF Pulse

4.1.2 Evolution of Ratio over Course of Run

Figure 4.4 shows the change in ratio over the course of an single run day (990128) from early in the campaign. There is a fairly steady shot-to-shot increase in the ratio over the course of the run. Since this is soon after the vent, this is likely also due to light hydrogen emitted from the walls (and from the RF antennae mentioned in the previous section), originating from water vapor. This "wall fueling", light hydrogen mixed with deuterium puffed into the plasma vessel, raises the H/D ratio.

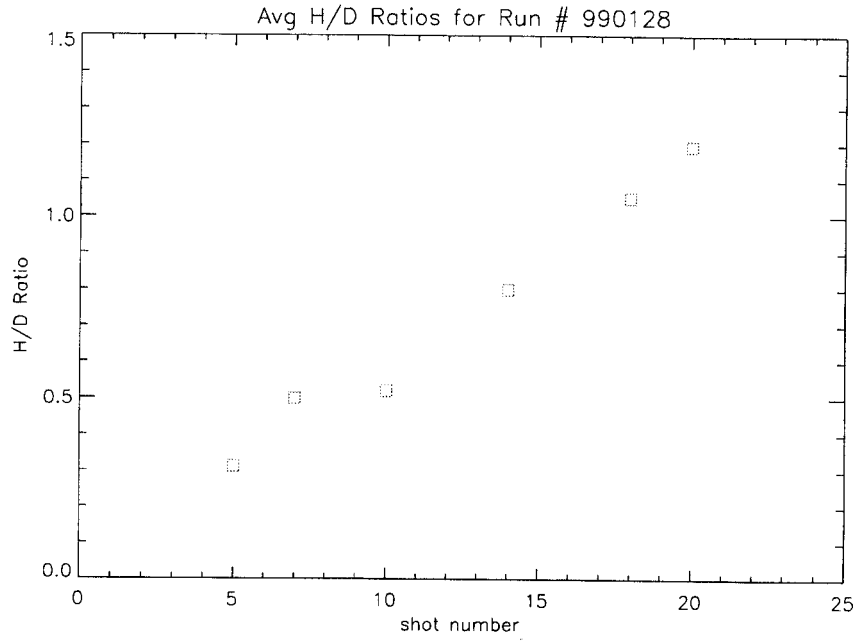

Figure 4.4: Shot averaged H/D ratios for run 990128. Average ratio increases from shot to shot

In the following day's run (990129, figure 4.5) the deuterium density is low due to problems with the gas puffing density feedback control, and fueling is almost entirely from the walls. Despite Electron Cyclotron Discharge Cleaning (ECDC) between each shot, there was a considerable increase of the H/D ratio with each shot particularly after a disruption at shot 008 decreasing slightly at the end of the run.

Figure 4.6 shows a later run (990422) after boronization of the vessel. The ratio remains between .04 and .06 during the course of the run, with only a slight trend of

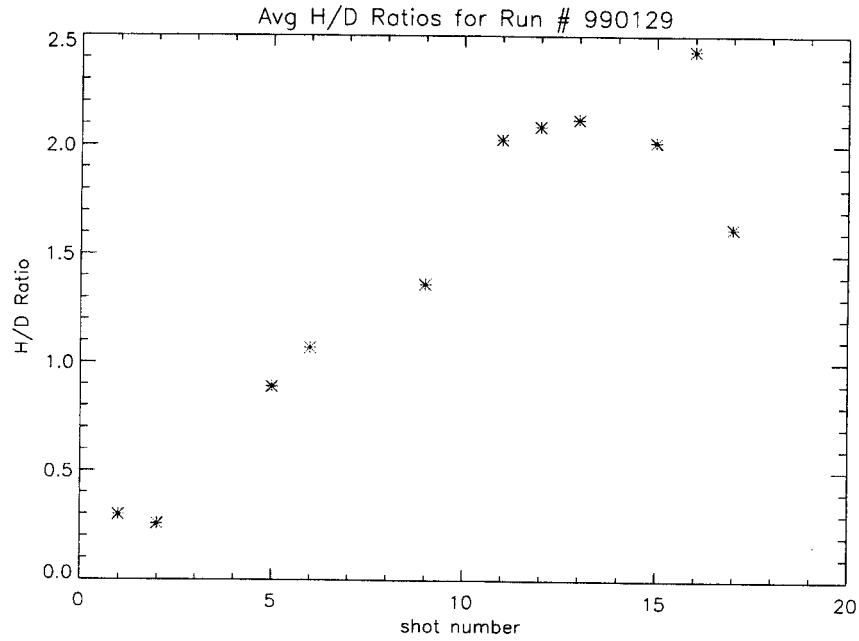

Figure 4.5: Shot averaged H/D ratios for run 990129, low plasma density

increase over the run.

4.1.3 Effect of ECDC and Boronization on Ratio

Figure 4.7 shows a plot of daily averages of the H/D ratio during the beginning of 1999's first run campaign. The daily average calculated is simply the run average of the individual averages of the ratio over each shot (eq. 3.18 over entire shot). There is a general decrease observed in the average of each run, while the average ratio value is observed to increase from shot to shot during each run day. Typically there are at least 2 hours of ECDC prior to each days run. The trend is a general linear decrease during the early running of the machine with the exception of 1/29 in which there was a considerably lower deuterium fraction for that day's run. Immediately following a three day weekend of constant ECDC in deuterium (D_2), there was a sharp drop in the ratio, followed by a similar trend of day to day decrease.

Figure 4.8 shows a series of shots before and after boronization, which was performed over four days, beginning on 2/13. This was followed by overnight ECDC in

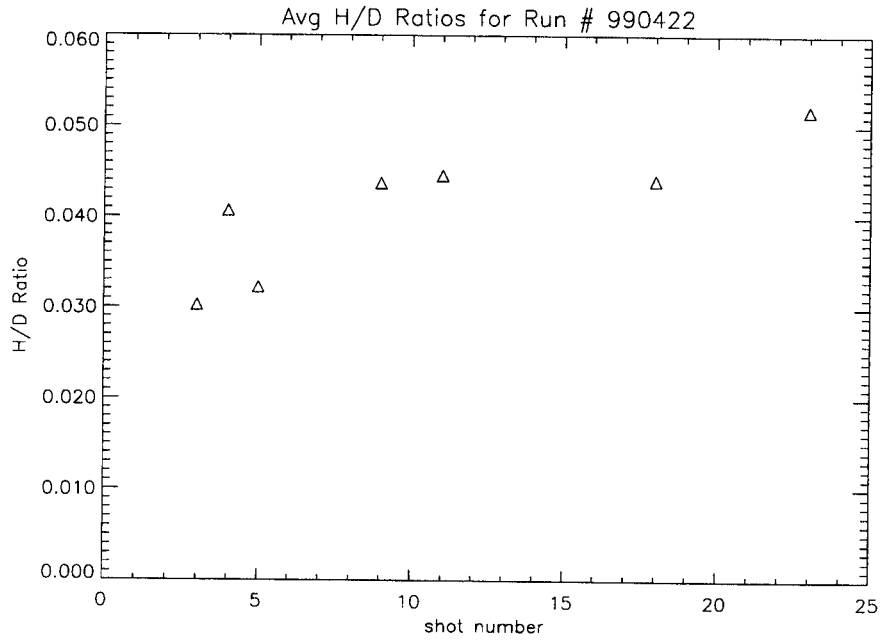

Figure 4.6: Shot averaged H/D ratios for run 990422, post boronization

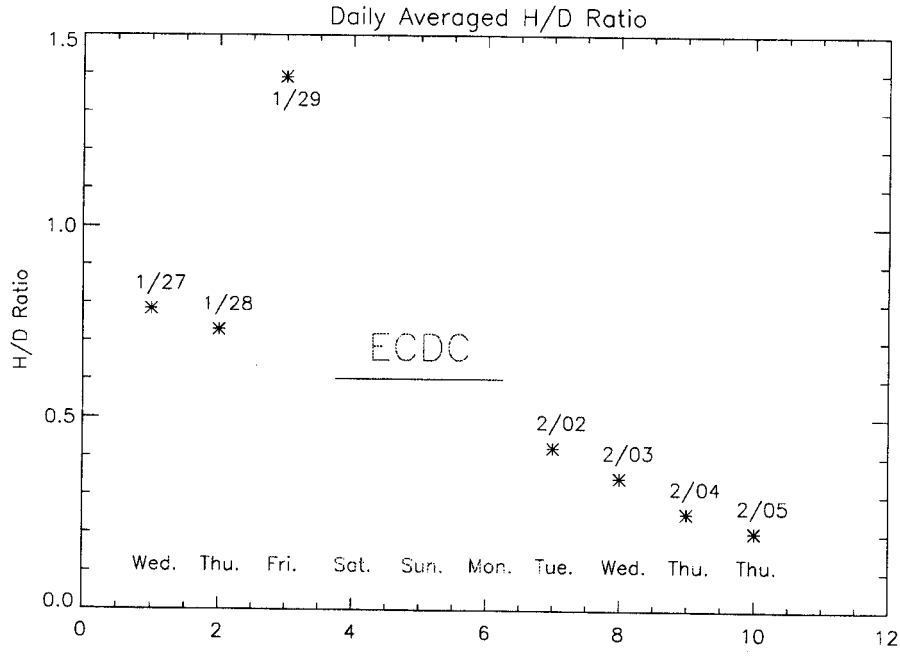

Figure 4.7: Daily run averages, before and after ECDC

He on 2/16, and finally two hours of ECDC in D_2 on the morning of 2/17, prior to the start of the run. There is a marked drop in the H/D ratio afterward, which remains between 2 and 5 %.

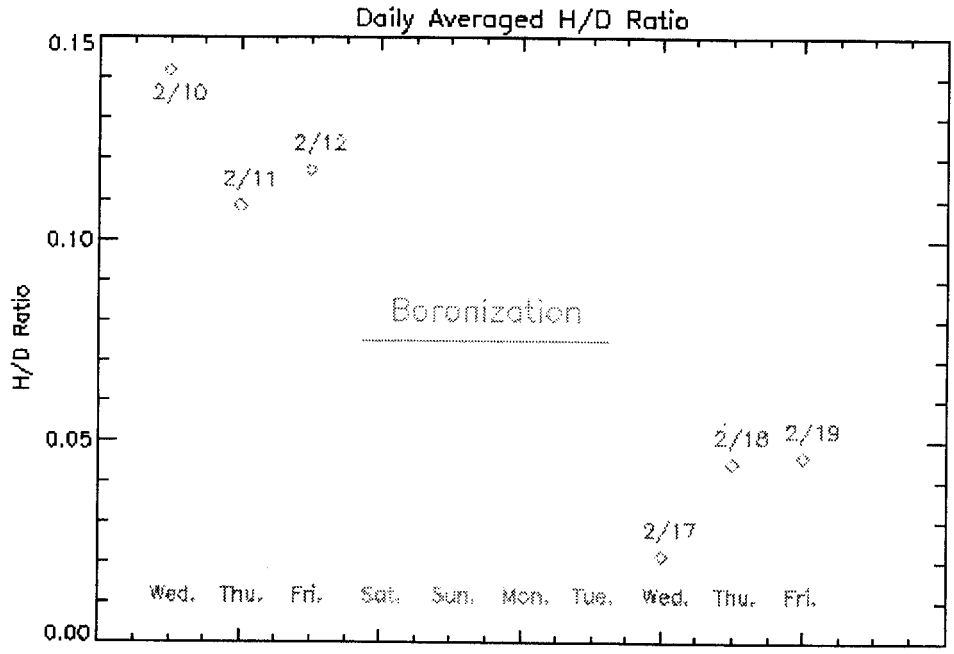

Figure 4.8: Daily run averages, before and after boronization

4.2 Effect of Minority Fraction on ICRF Heating

4.2.1 Theory

Figure 4.9 shows a simplified predicted single-pass RF absorption curve as a function of the minority concentration. Below the η_{crit}, in the minority regime, the RF aborption decreases due to the lack of a solution to the real component of the kinetic dispersion relation (eq. 2.21). the exact behavior in this regime is not clearly understood, hence the dashed line. What is significant is that rf damping is at a maximum at $\eta = \eta_{crit}$, and is ~ 0 at $\eta = 0$. At values significantly above η_{crit}, the curve is roughly proportional to $1/\eta$, in accordance with the Fluid Theory regime of eq. 2.19

(figure 2.1).

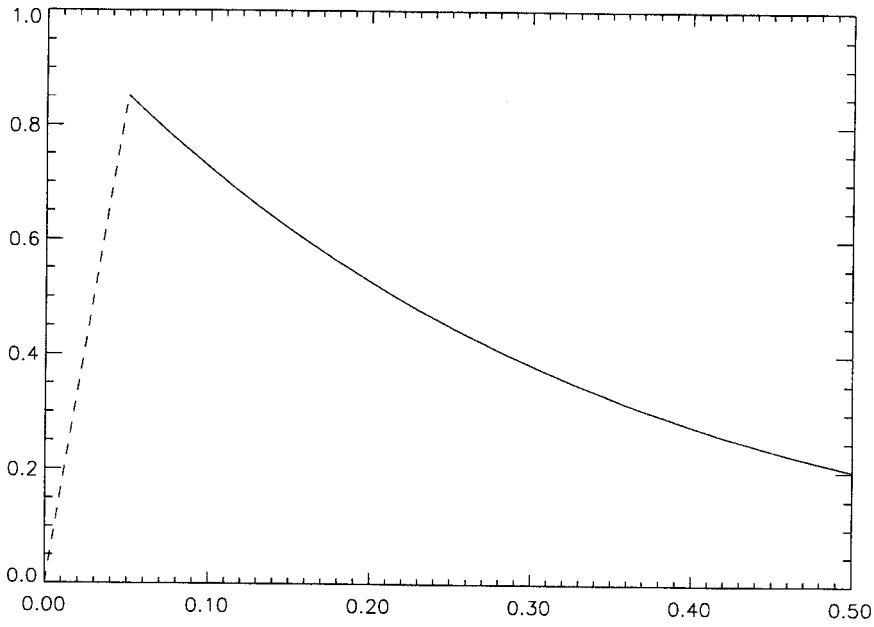

Figure 4.9: Kinetic theory prediction of single-pass RF absorption, Dashed lines indicate uncertainty of RF damping in the minority regime ($\eta < \eta_{crit}$)

For a single pass of the RF wave through the plasma[17], the absorption and transmission coefficients are given by:

$$\text{RF absorption} = A = 1 - e^{-2\epsilon} \tag{4.1}$$

$$\text{RF transmission} = 1 - A = e^{-2\epsilon} \tag{4.2}$$

where:

$$2\epsilon = \frac{|E_L|^2}{|E_Y|^2} \frac{\omega_{p_i}}{c} \frac{n_{min}}{n_{Maj}} \frac{Z_{min} m_{Maj}}{Z_{Maj} m_{min}} R_o \tag{4.3}$$

4.2.2 Stored Energy vs. H/D Ratio

To experimentally determine the fraction of RF power absorbed, α, one must know the total energy stored in the plasma. This is calculated automatically from EFIT

data and found in the ANALYSIS data tree [18].

During the run campaigns of 1999, data were collected for many plasmas, of which over 150 were heated by RF. There is a sufficient number of shots (N=75 for L-mode and N=95 for H-mode) to perform a fairly detailed analysis of the data.

Figure 4.10 through 4.12 show the plasma stored energy increase in joules plotted vs. the H/D ratio, η. The RF ranges from 1.25 to 2.50 MW. The stored energy and the H/D are both averaged over the time of the RF pulse. The plasma current is 800 kA in all cases.

In figure 4.10 the RF input power is between 1.00 and 1.25 MW. There are no data points for η values between ~ 0.1 and ~ 0.18. This gap is primarily due to differences between pre- and post-boronization conditions. Also there was no RF power on the few shots with η values in that range The points form a broad envelope describing a general $1/\eta$ trend down to about 0.05. where it shows a very slight tendency to level off towards a maximum. There are a few outliers present, two large energy values just above $\eta = 0.05$ and one small energy value just below $\eta = 0.05$. While they fall generally in the expected pattern, they are outside of the envelope established by the rest of the points. In any case, there are too few points in the desired range to establish the predicted cutoff at $\eta = 0.05$ definitively.

Figure 4.11 shows stored energy values for RF input power input of 1.25 to 1.50 MW. It shows a similar trend (and gap between 0.1 and 0.2) The envelope is wider in this case, however, and it is not clear whether the apparent levelling at $\eta = 0.5$ is real or an artifact due to the broader envelope. A few outliers below the envelope at $\eta \sim 0.4$ would suggest that a maximum is present, but again, there are too few points to be conclusive.

Figure 4.12 shows a very narrow envelope, which describes a fairly smooth curve in the $1/\eta$ region between 0.05 and 0.10. Unfortunately, there are no values significantly below $\eta = 0.05$, There is no evidence of the curve levelling towards a maximum in this plot.

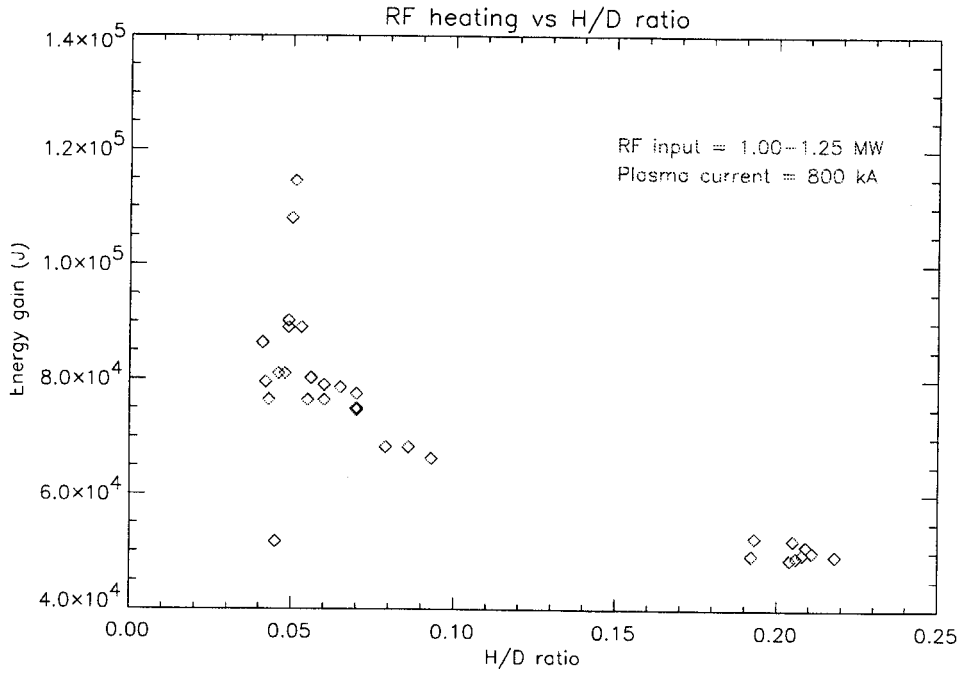

Figure 4.10: Plasma stored energy vs. H/D ratio, RF input 1.00-1.25 MW

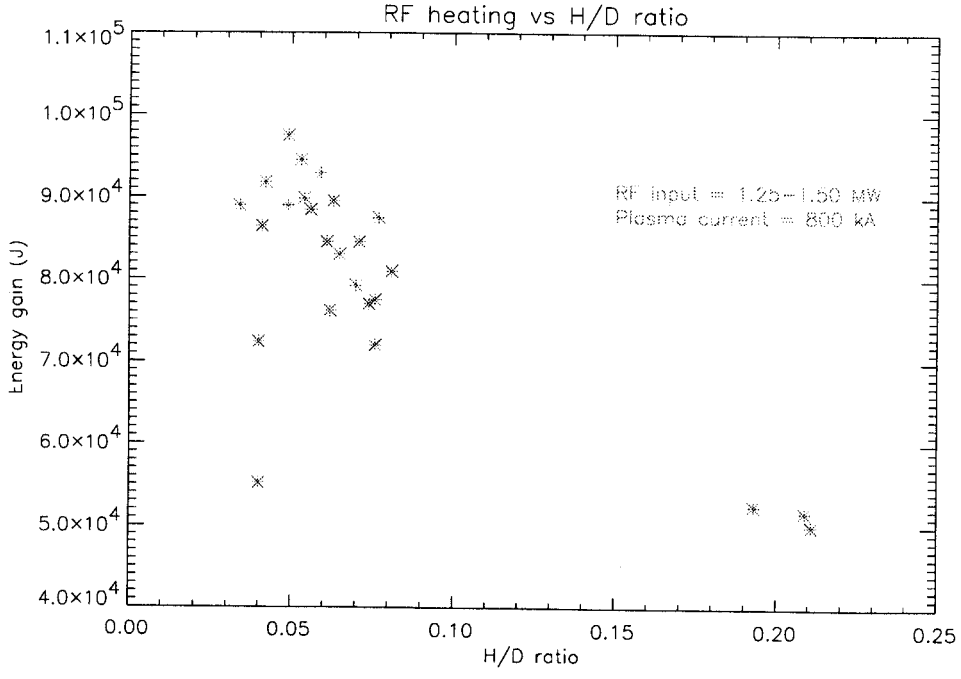

Figure 4.11: Plasma stored energy vs. H/D ratio, RF input 1.25-1.50 MW

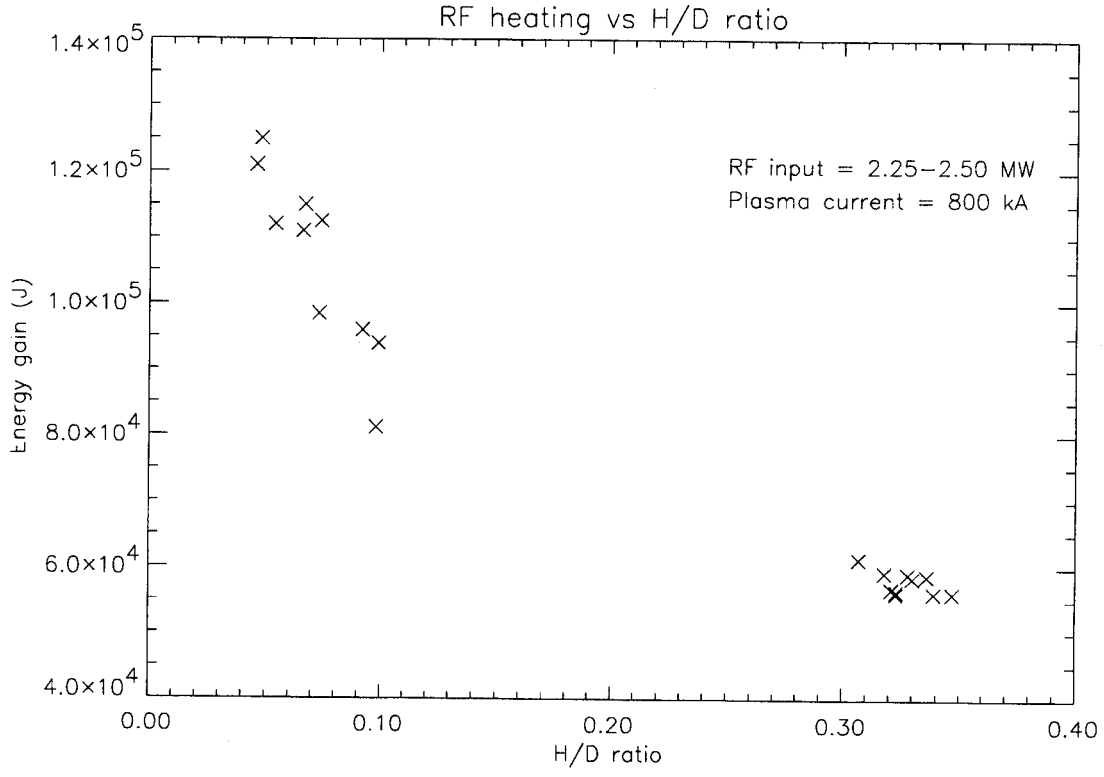

Figure 4.12: Plasma stored energy vs. H/D ratio, RF input 2.25-2.50 MW

4.2.3 Calculation of RF Absorption via ITER 89 Scaling

While useful, these plots represent only a rudimentary attempt to determine a relationship between RF absorption and η. Only relative RF absorption vs. η may be inferred by this approach. There are many other variables besides the RF Input. Though all shots examined have the same plasma current (800 kA), there is considerable variation in ohmic power, since the plasma resistivity is proportional to $kT_e^{-3/2}$. Also, no discrimination is made between normal (L-mode), and enhanced (H-mode) confinement. To group by ohmic power and confinement mode would reduce the number of data points per graph to an insufficent number as to provide adequate statistics. A more explicit method to calculate RF absorption is needed.

To more accurately determine the total RF absorption, α, with respect to η. we must calculate α explicity. First, we measure the plasma stored energy. Next we note that, in steady state, the total stored energy measured in the plasma is the product of the total power input (P_{tot}) and the confinement time τ:

$$\text{Stored Energy} = W_p = \tau P_{tot} \tag{4.4}$$

where the total power input to the plasma is:

$$P_{tot} = P_\Omega + \alpha P_{RF} \tag{4.5}$$

Since τ represents a second unknown in the equation in addition to α, one obtains a value for τ by using the ITER 89 empirical L-mode scaling law [19]:

$$\tau_{\text{ITER 89}} = 0.48 I_p^{0.85} R_0^{1.2} a^{0.3} \kappa^{0.5} n_e^{0.1} B_{tor}^{0.2} m_D^{0.5} P_{tot}^{-0.5} \tag{4.6}$$

where I_p is the plasma current in MA, R_0 and a are the major and minor radii in meters, n is the plasma density in 10^{20} m^{-3}, B is the toroidal magnetic field in Tesla, m_D is the mass of majority ion in atomic mass units (amu). and P_{tot} is the total

power input to the plasma in MW (eq. 4.5). The energy confinement is then:

$$\tau_E = H\tau_{\text{ITER 89}} \tag{4.7}$$

With these parameters known, one can now solve for α in terms of W:

$$\alpha(meas.) = \frac{1}{P_{RF}}\left[(\frac{217}{\kappa})(\frac{W}{H})^2 I_p^{-1.7} R^{-2.4} a^{-0.3} n_e^{-0.2} B^{-0.4} - P_\Omega\right] \tag{4.8}$$

where H is a dimensionless scaling factor that separates L-mode from H-mode. Typically H is ~ 1 for L-mode and for H-mode $1.0 \leq H \leq 2.2$ [20].

Figures 4.13 and 4.16 represent the application of equation 4.8 to shots performed since the installation of the spectrometer. While there is a definite pattern in each confinement mode, a pattern that follows the predicted curve of figure 4.9, there is a lot of variation in the y axis values. Much of the variation is from shot to shot, suggesting that other unknowns are having an effect.

Of particular interest is that the upper edge of the envelope describes the prediced single-pass curve fairly well, The other points tend to fill the area beneath the predicted curve. This is likely due to variations in H.

It is helpful in this case to bin and average the results. The range of η is divided into bins of width j with a total of n bins:

$$n = \frac{\eta_{max}}{j}$$

All of the points within a given bin (η_{n-1} to η_n) are then averaged:

$$\overline{\alpha}_n = \frac{\sum_{\eta_{n-1}}^{\eta_n} \alpha(\eta)}{N_{\eta_n}} \tag{4.9}$$

while the X axis bins are simply the mid points between each bin division [21]:

$$\overline{\eta}_n = \frac{\eta_n + \eta_{n-1}}{2} \tag{4.10}$$

L-mode

Figure 4.13 shows the calculated value of α plotted against η for L-Mode shots taken in 1999. Values for η range from ~ 0.03 to ~ 0.50. The upper edge roughly describes the $1/\eta$ portion of the curve.

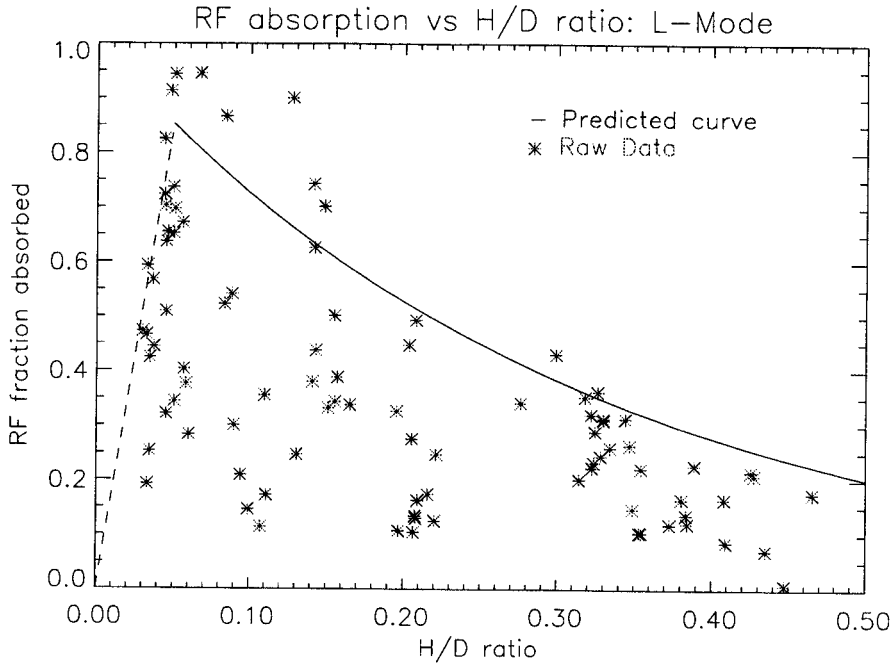

Figure 4.13: RF absorption (α) for L-mode shots

Figure 4.14 shows the same data plotted with η values binned in intervals of 0.01 (1%). While there is still a fairly broad envelope, the upper edge is less curved and appears to be transitioning between describing a rational ($y = 1/x$) curve and a linear ($y = b - mx$) function. There is no evidence of levelling toward a maximum near $\eta = \eta_{crit}$.

In Figure 4.15, η is binned at intervals of 0.02 (2%), The envelope is narrowing, but is still broad. particularly at the lower end of the η axis. There is a slightly greater trend towards linearity as well. As in figure 4.14 there is little or no evidence of levelling toward a maximum near $\eta = \eta_{crit}$.

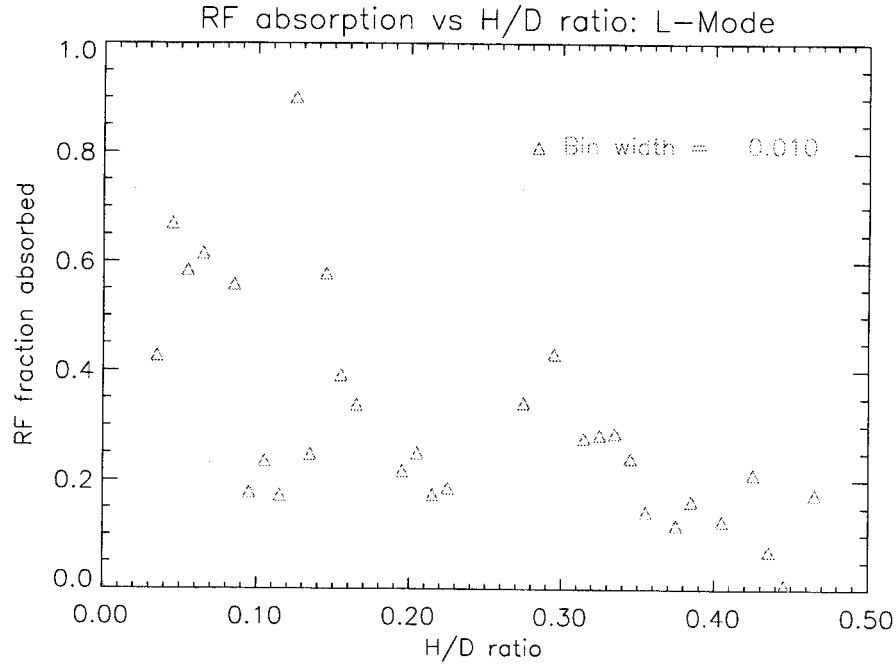

Figure 4.14: L-mode α vs. η, binned at 1%

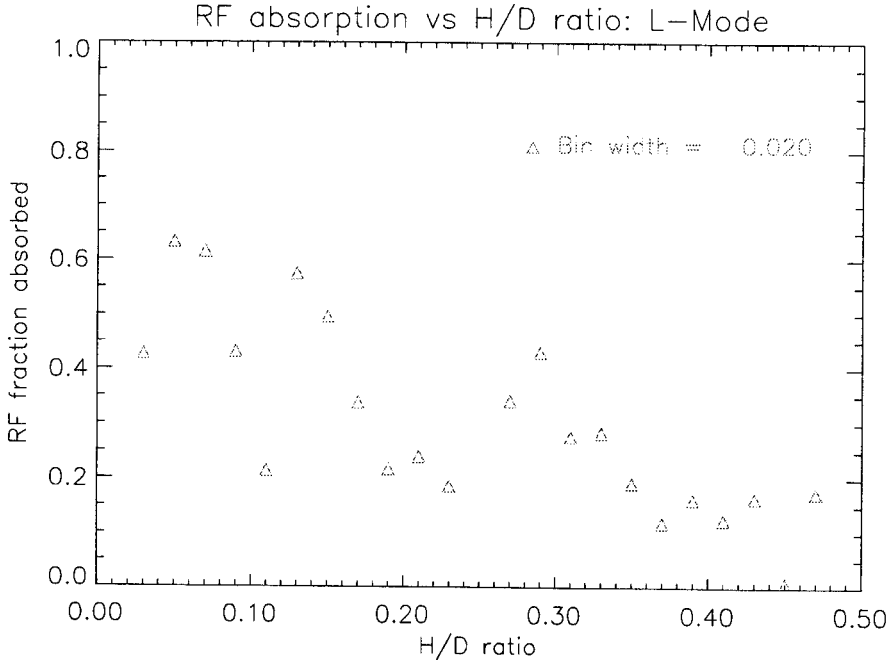

Figure 4.15: L-mode α vs. η, binned at 2%

H-mode

For enhanced-confinement or "H-mode" shots, τ from eq. 4.6 is multiplied by a scaling or "H" factor. A difficulty encountered when calculating α for H mode shots, is the uncertainty in the value of this H factor:

$$H = \frac{\tau_E}{\tau_{\text{ITER 89}}}$$

where, again in steady state:

$$\tau_E = \frac{W}{P_\Omega + \alpha P_{RF}}$$

which gives two equations (4.8, 4.7) but three unknowns (H, τ_E, α). It is necessary to assume a value for H. For enhanced confinement, this factor can vary from 1.0 to 2.2. Calculations in this section will assume H to be fixed at 1.8.

Figure 4.16 shows the calculated value of α plotted vs η for H-Mode shots taken in 1999. Values for η range from $\sim$ 0.025 to $\sim$ 0.010, with a sharp drop off in α for η values of 0.08 to 0.1. This drop, along with the lack of data points in H-mode for values of η greater than $\sim$ 0.01 suggest that it is difficult to achieve H-mode confinement if the minority concentration exceeds 0.01, or 10%.

It is difficult to determine whether there is a $1/\eta$ curve described by the upper edge of the envelope, as there are too few data points present. There is, however, a slightly greater trend towards a maximum at $\eta = 0.05$ than in the L-mode plots of α vs. η but this is still inconclusive.

Figure 4.17 shows η binned at 0.0025 (0.25%). The envelope is beginning to show signs of a maximum at $\eta = 0.05$. The lack of points for η above 0.1 make it difficult to establish a $1/\eta$ curve in the region above $\eta = 0.05$

Figure 4.18 shows η binned at 0.02. This is the upper limit of bin width, as the critical η value is 0.05 and larger bins would not allow observation of the behavior of α around η_{crit}. Even though there are more data points for H-mode plasmas than for L-mode, they are all clustered below 0.01. Therefore this graph has only has four

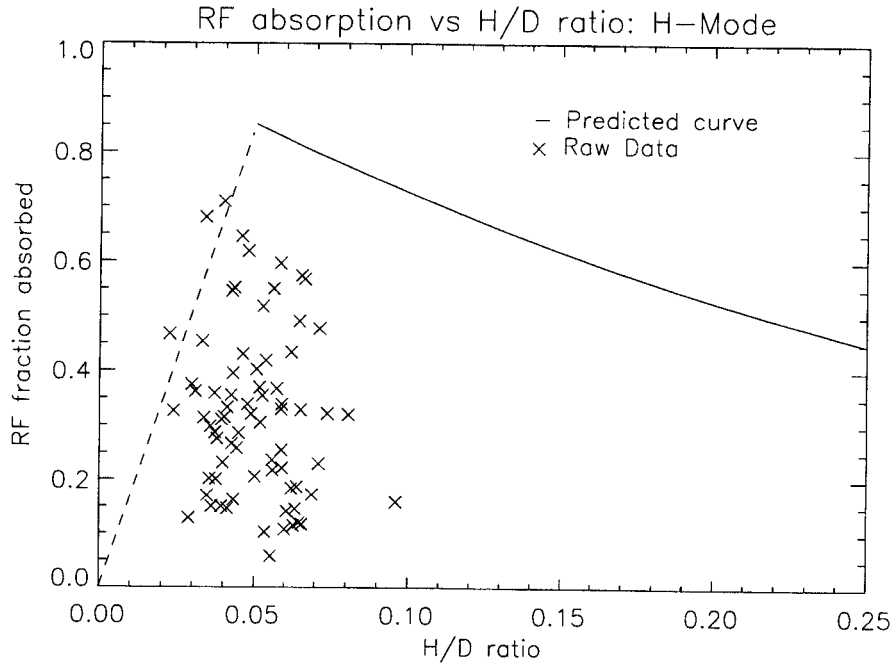

Figure 4.16: RF absorption (α) for H-mode shots

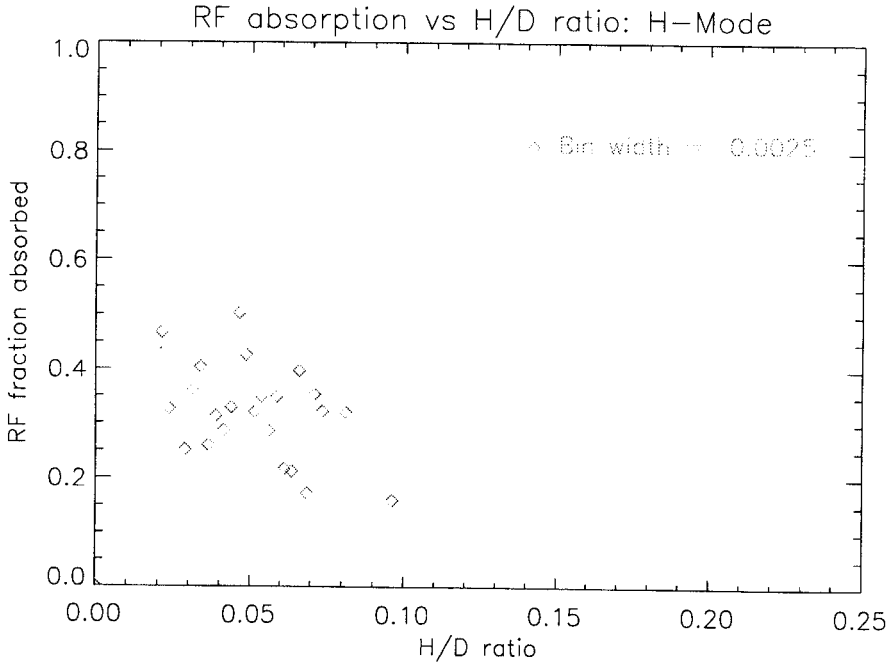

Figure 4.17: H-mode α vs. η, binned at 0.25%

points. While a maximum is somewhat visible at $\eta = .05$, there are too few data points to determine whether this is real, or an artifact of the binning process.

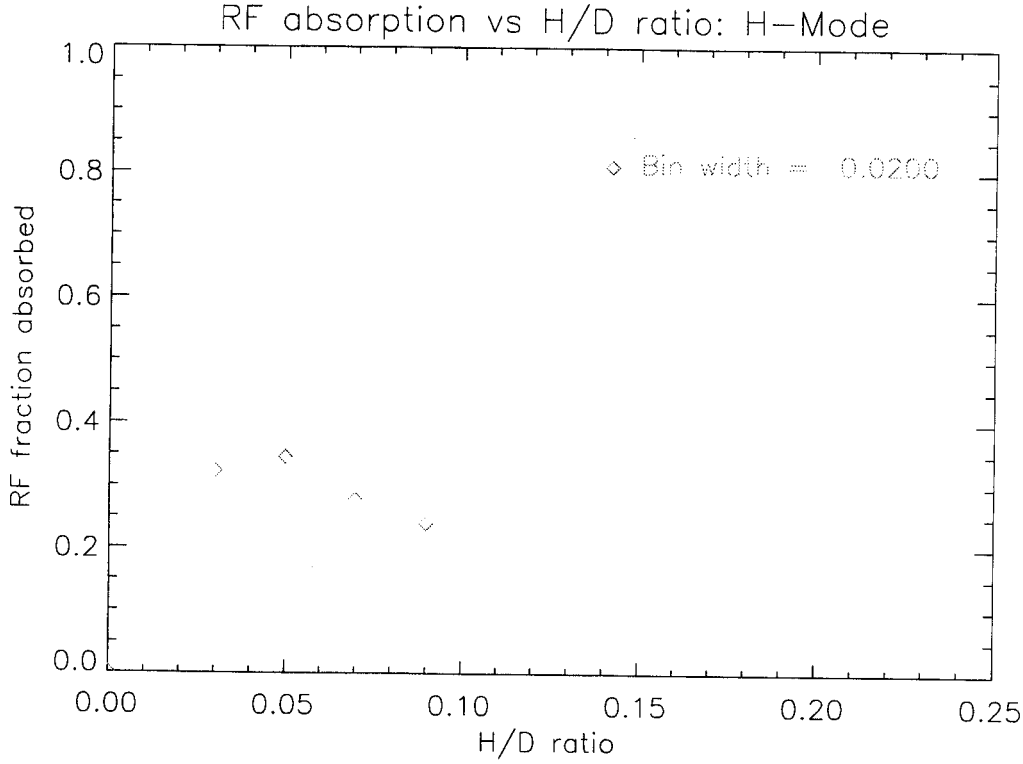

Figure 4.18: H-mode α vs. η, binned at 2%

4.2.4 Calculation of RF Absorption via Modulation Method

An alternative method by Wukitch et al [22] in 1998 explores the total RF absorption via modulation of the RF input. This method observes the slope of the plasma stored energy curve at the end of an RF pulse. The change in stored energy of the plasma $(\partial W_p/\partial t)$ is governed by the global power balance equation:

$$\frac{\partial W_p}{\partial t} = \alpha P_{RF} + P_\Omega - P_{rad} - \frac{W_p}{\tau_E} \tag{4.11}$$

If one takes the time of RF shutoff as $t = 0$, and the time interval of observation

is small ($\Delta t << \tau_E$), then the total RF power absorbed by the plasma is given by:

$$P_{RF_{abs}} = \left.\frac{\partial W_p}{\partial t}\right|_{t\to 0^-} - \left.\frac{\partial W_p}{\partial t}\right|_{t\to 0+} \tag{4.12}$$

Since the derivative is taken over a finite time interval ($\Delta t > 0$) as opposed to instantaneously ($\Delta t \to 0$), this will be a slight underestimate of the total RF power absorbed [23]. Once total amount of absorbed power is known, one can calculate α from the input power. The fraction of RF power absorbed is then:

$$\alpha = \frac{P_{RF_{abs}}}{P_{RF_{in}}} = \frac{1}{P_{RF_{in}}}\left[\left.\frac{\partial W_p}{\partial t}\right|_{t\to 0^-} - \left.\frac{\partial W_p}{\partial t}\right|_{t\to 0+}\right] \tag{4.13}$$

Also, it is worth noting that this study was done prior to the implementation of our spectrometer, and the minority fraction was calculated by fast neutral particle analysis [24]. In addition, the plasma stored energy was calculated from diamagentic loop data, as opposed to the EFIT method referenced in section 4.2.2.

Figure 4.19 shows a plot of the fraction of RF absorption vs. ^{1}H minority concentration. The number of data points and the range of data are low in this case. There is no real maximum visible and what vague trend is apparent appears to be a general linear increase with the ratio. Also of note is that the minority concentration is expressed as $H/H+D$ as opposed to H/D in our own measurements. If one lets $H/H+D = \eta\prime$, then $H/D = \eta = \eta\prime/(1-\eta\prime)$. This will shift the points to the left by a factor of 1.05 to 1.10 in this region.

Figure 4.20 is a plot of the fraction of RF absorption vs. $\eta\prime$ in high field shots where ^{3}He is used as the minority species. These points follow the predicted curve of 4.2.1 fairly well. A maximum is clearly visible at $\sim 0.020 - 0.022$. This agrees with the predicted value of η_{crit} (~ 0.020) for ^{3}He using equation 2.23.

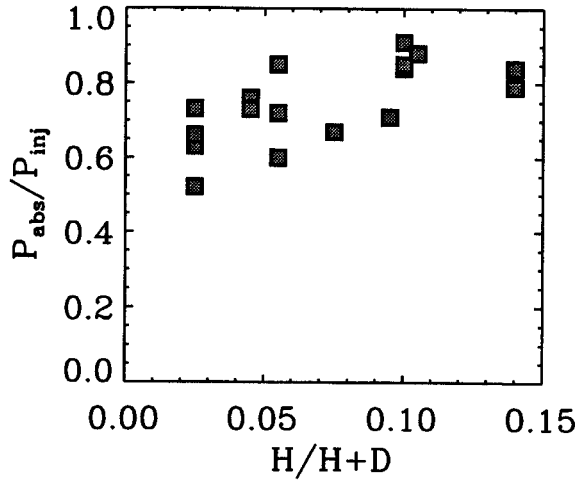

Figure 4.19: Plot of RF absorption calculated by modulation of the RF signal (^{1}H minority)

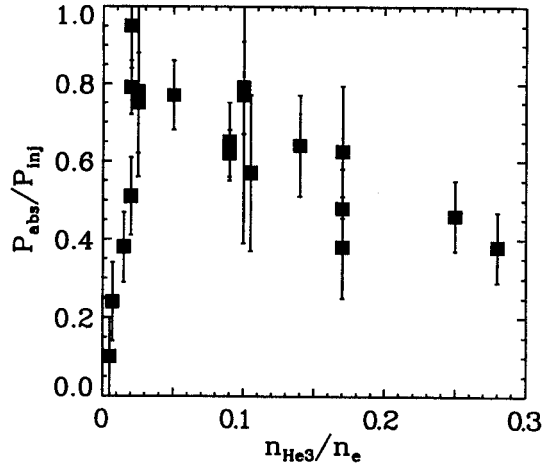

Figure 4.20: Plot of RF absorption calculated by modulation of the RF signal (^{3}He minority)

4.3 Future Work

All shots up to the present have employed passive control of the H/D ratio by means of baking, electron cyclotron discharge cleaning (ECDC), and boronization of the vacuum vessel prior to a run. This has resulted in ^{1}H minority concentrations as low as 2%, with ^{1}H introduced in the plasma via wall fueling from hydrogen bearing compounds in the invessel components and vessel walls.

Section 4.2 shows that the RF absorption is maximum for H/D ratios of $\sim$ 5%, and drops off as H/D increases. To maintain maximum RF heating efficiency, active control methods will be necessary to maintain the minority concentration as close as possible to the optimum value.

Chapter 5

Summary and Conclusions

In summary, the following was learned from implementation of the spectrometer:

- The weighted average method is the most accurate and efficient way of calculating the H/D Ratio.
- The Curvefit routine is useful in limited circumstances, using horizontal polarizing filters. primarily to understand the contributions of each spectral line component.
- Horizontal polarization provides the most usable spectrum for the above methods.

In addition, these trends in the H/D ratio were observed over the first run campaign of 1999:

- H/D Ratio tends to increase over the course of a shot, particularly during the RF pulse.
- While shot-averaged H/D ratio tends to increase over the course of a run, the daily average tends to decrease from run to run, particularly when overnight ECDC is applied.

- Boronization and extensive periods of ECDC will produce significant reductions in the H/D ratio.

- Application of ECDC and boronization, ultimately result in H/D ratios of 2 to 4 %. This should be low enough to allow control of the ratio via active methods (puffing, etc.)

- Absorbed RF power as a function of the H/D ratio tentatively follows the predicted curve fairly well. However, there are too few data points for this to be conclusive.

The H-α/D-α spectrometer has proven to be a useful tool for plasma diagnostic work on Alcator C-Mod. In addition to providing information for RF heating, the H/D ratio can provide important clues about conditions within the vacuum vessel and also at the plasma edge.

Chapter 6

References

1. Betti, R.; MIT course 22.62; "Fusion Energy"; Course lecture notes: c1999; sec. 15.2:15.6
2. Ibid., sec. 15.7:15.8
3. Hutchinson, I; MIT course 22.62; "Fusion Energy"; Course lecture notes: c1998; sec. RF Heating, p 70
4. Wesson, John, "Tokamaks /2nd ed.", Oxford : New York : Clarendon Press ; Oxford University Press, 1997.; pp. 249-252
5. Betti, R.; MIT course 22.62; "Fusion Energy"; Course lecture notes: c1999; sec. 16.2
6. Wesson, John, "Tokamaks /2nd ed.", Oxford : New York : Clarendon Press ; Oxford University Press, 1997.; pp. 253:255
7. Betti, R.; MIT course 22.62; "Fusion Energy"; Course lecture notes: c1999; sec. 16.5
8. Brehm, John J.; Mullin, William J; "Introduction to the structure of matter ; a course in modern physics"; New York ; Wiley, c1989.; pp. 152-154
9. Fastie, Wm. G.; "A Simple Plane Grating Monochromator"; Journal of the Optical Society of America; Volume 42, No. 9; Sept. 1952

10. Terry, James; Personal Consultation; Aug. 1999

11. Brehm, John J.; Mullin, William J; "Introduction to the structure of matter ; a course in modern physics"; New York ; Wiley, c1989.; pp. 377-379

12. Montgomery, Douglas C.; Runger, George C.;"Applied Statistics and Probability for Engineers"; New York ; Wiley, c1994; pp. 173-174

13. Chen, Francis F.;"Plasma Physics and Controlled Fusion Vol. 1"; New York and London; Plenum; 2nd Ed. c1984; pp. 226-229

14. Rice, John; Personal Consultation; Feb. 1999

15. Marmar, Earl; Personal Consultation; Feb. 1999

16. Betti, R.; MIT course 22.62; "Fusion Energy"; Course lecture notes: c1999; sec. 8.6

17. Hutchinson, I; MIT course 22.62; "Fusion Energy"; Course lecture notes: c1998; sec. RF Heating, p 70

18. Lao, L. L.; St. John, H.; Stambaugh, R. D,; Kellman, A. G.; Pfeiffer, W.; "Reconstruction of Current Profile Parameters and Plasma Shapes in Tokamaks"; Nuclear Fusion; Vol. 25; No,2; c1985

19. Betti, R.; MIT course 22.62; "Fusion Energy"; Course lecture notes: c1999; sec. 8.4-8.5

20. Ibid.; sec 8.5

21. Montgomery, Douglas C.; Runger, George C.; "Applied Statistics and Probability for Engineers"; New York ; Wiley, c1994; pp. 8,16

22. Wukitch, S., Bonoli, P.T., Phillips, C.K., et al.,; "ICRF Heating Experiments in Alcator C-Mod,"; 17th IAEA Fusion Energy Conference; Yokohama, Japan, 19-24 October 1998; Published in Extended Synopses IAEA-CN-69 Proceedings; p. 88.

23. Ibid.

24. Wesner F., Prozesky VM., Behrisch R., Staudenmaier G.; "Measurement of fast particles in front of the ICRH-antenna of ASDEX."; Fusion Engineering and Design; vol.12; no.1-2; April 1990; pp.193-6

Made with LaTeX version 2ε